

Numerical analysis of fan noise for the NOVA boundary-layer ingestion configuration

Original

Numerical analysis of fan noise for the NOVA boundary-layer ingestion configuration / Romani, Gianluca; Ye, Qingqing; Avallone, Francesco; Ragni, Daniele; Casalino, Damiano. - In: AEROSPACE SCIENCE AND TECHNOLOGY. - ISSN 1270-9638. - 96:(2020), p. 105532. [10.1016/j.ast.2019.105532]

Availability:

This version is available at: 11583/2976949 since: 2023-03-14T11:30:50Z

Publisher:

Elsevier

Published

DOI:10.1016/j.ast.2019.105532

Terms of use:

This article is made available under terms and conditions as specified in the corresponding bibliographic description in the repository

Publisher copyright

(Article begins on next page)



Numerical analysis of fan noise for the NOVA boundary-layer ingestion configuration

Gianluca Romani*, Qingqing Ye, Francesco Avallone, Daniele Ragni, Damiano Casalino

Delft University of Technology, 2629 HS, Delft, the Netherlands

ARTICLE INFO

Article history:

Received 29 July 2019

Received in revised form 7 October 2019

Accepted 31 October 2019

Available online 7 November 2019

Keywords:

Lattice-Boltzmann method

Turbofan

Boundary-layer ingestion

Aerodynamics

Aeroacoustics

ABSTRACT

Aim of this paper is to investigate the effects of the turbulent flow developing over a fuselage on fan noise for BLI embedded propulsion systems. Such configurations can suffer from inlet flow distortions and ingestion of turbulence at the fan plane with consequent impact on both broadband and tonal fan noise. The analysis is performed on a modified version of the Low-Noise NASA SDT fan-stage integrated into the ONERA NOVA fuselage in order to reproduce the NOVA BLI configuration. The numerical flow solution is obtained by solving the explicit, transient and compressible lattice-Boltzmann equation implemented in the high-fidelity CFD/CAA solver Simulia PowerFLOW®. The acoustic far-field is computed by using the Ffowcs-Williams & Hawkins integral solution applied to a permeable surface. All simulations are performed for an operating condition representative of a take-off with power cut-back. Installation effects due to the BLI configuration are quantified by comparison with an isolated configuration of the modified Low-Noise SDT fan-stage at the same operating condition. It is found that the BLI fan-stage, which is not optimal, is characterized by strong azimuthal fan blade loading unsteadiness, less axisymmetric and coherent rotor wake tangential velocity variations and higher levels of in-plane velocity fluctuations compared to the isolated engine. This resulted in no distinct tonal components and higher broadband levels in the far-field noise spectra, as well as in an increment of cumulative noise levels up to 18 EPNdB. This study, which represents the first high-fidelity CFD/CAA simulation of a full-scale aircraft geometry comprehensive of a BLI fan/OGV, provides with a clear understanding of the change of the noise sources in BLI integrated configurations.

© 2019 The Authors. Published by Elsevier Masson SAS. This is an open access article under the CC BY-NC-ND license (<http://creativecommons.org/licenses/by-nc-nd/4.0/>).

1. Introduction

1.1. Background

In order to deal with the increasingly stringent aviation regulations for pollution and noise impact [1], the use of Ultra-High Bypass Ratio (UHBR) engines on next generation aircraft is receiving more attention due to their lower jet core flow velocity and noise emissions, and enhanced propulsive efficiency compared to low- and high-bypass turbofans. Such engines have a relatively larger fan diameter with consequent increase of the blade tip speed for constant cruise velocity. As a consequence of the jet noise reduction and increase of the blade size, fan noise becomes the primary source of noise for these configurations [2]. Moreover, their actual employment on future aircraft raises new integration challenges,

requiring special designs to install such large and heavy engines minimizing their impact on aircraft performances.

In the last two decades, many researchers have put their efforts on developing novel aircraft configurations suited for UHBR engines integration [3–6]. In this scenario, four different NOVA (Nextgen ONERA Versatile Aircraft) aircraft geometries have been designed by ONERA in last few years with a particular emphasis on engine integration: (i) a baseline architecture with wide lifting fuselage, under-wing engines, high wing aspect ratio and downward oriented winglets, (ii) a gull wing layout characterized by an increased dihedral angle in the wing inboard position to limit landing gears length, (iii) a podded configuration with engines mounted on the aft fuselage side, and (iv) a Boundary-Layer Ingestion (BLI) configuration with engines installed on the aft fuselage side and ingesting the boundary-layer convecting over the fuselage [5]. Starting from these studies, the present work, which takes place in the framework of the European Commission project ARTEM (Aircraft noise Reduction Technologies and related Environmental iM pact), focuses on the last configuration.

* Corresponding author.

E-mail address: G.Romani@tudelft.nl (G. Romani).

Nomenclature

Roman symbols

a	=	Speed of sound
C	=	Collision operator
$c_T \tilde{V}^2$	=	Sectional thrust coefficient
f	=	Frequency
g	=	Particle distribution function
g^{eq}	=	Particle distribution function at equilibrium
H	=	Shape factor
\mathbf{i}_{x_e}	=	Engine axis unit vector
M	=	Mach number
\mathbf{n}	=	Airfoil contour outward-pointing normal
p	=	Static pressure
r	=	Fan radial coordinate
R	=	Fan radius
R_s	=	Hemisphere radius
S	=	Ray-hemisphere intersection
\tilde{S}	=	Reflected ray-hemisphere intersection
t	=	Time
T	=	Fluid temperature
u	=	Wall-parallel fluid velocity
U	=	Fluid velocity magnitude
\mathbf{v}	=	Particle velocity vector
V	=	Fan blade sectional velocity magnitude
\tilde{V}	=	Normalized fan blade sectional velocity magnitude
w	=	Wall-normal fluid velocity
\mathbf{x}	=	Particle position vector
x, y, z	=	Cartesian coordinates
y^+	=	Non-dimensional wall-distance in viscous units

Greek symbols

α	=	Aircraft angle of attack
γ	=	Aircraft glide angle
δ	=	Boundary-layer thickness
η_f	=	Fan isentropic efficiency
θ	=	Directivity angle along each microphones arc
ρ	=	Fluid density
Σ	=	Airfoil contour
τ	=	Relaxation time
T	=	Fan rotation period

ϕ	=	Meridian position of each microphones arc
φ	=	Aircraft pitch angle
Ω	=	Fan angular velocity

Subscripts

∞	=	Free-stream conditions
tip	=	Fan blade tip conditions
a	=	Aircraft reference frame
e	=	Engine reference frame
g	=	Ground-fixed reference frame
k	=	k -th ground microphone
j	=	j -th discrete particle velocity direction

Superscripts

'	=	Flow quantity fluctuation
$\bar{\cdot}$	=	Time-averaged flow quantity
i	=	i -th flight sub-segment

Acronyms

BPF	=	Blade-Passing Frequency
BLI	=	Boundary-Layer Ingestion
CAA	=	Computational Aero-Acoustics
CFD	=	Computational Fluid Dynamics
EPNL	=	Effective Perceived Noise Level
FAR	=	Federal Aviation Regulations
FPR	=	Fan Pressure Ratio
FE	=	Fine Equivalent
FW-H	=	Ffowcs-Williams & Hawkings
LBM	=	Lattice-Boltzmann Method
LRF	=	Local Reference Frame
NBN	=	Narrow-Band Noise
NOVA	=	Nextgen ONERA Versatile Aircraft
OGV	=	Outlet Guide Vane
PSD	=	Power Spectral Density
PWL	=	Power Level
SD	=	Standard Deviation
SDT	=	Source Diagnostic Test
UHBR	=	Ultra-High Bypass Ratio
VLES	=	Very Large Eddy Simulation
VR	=	Variable Resolution

1.2. Overview of BLI technology and state-of-the-art

BLI propulsion systems aim at reducing the required propulsive power compared to conventional tube-and-wing configurations [5–8]. Its theoretical propulsive benefit is based upon the possibility to reduce: (i) the overall aircraft mass and drag, due to the nacelle pylon removal and the lower wetted surface area; (ii) the power dissipation in the flow field, by reducing the exhaust jet wasted kinetic energy and filling-in the airframe wake velocity defect. Moreover, with BLI, the propulsion system is partially or completely shielded by the airframe, depending on the placement of the engine, thus yielding to a potential noise reduction due to acoustic shielding. However, many drawbacks should be addressed before quantifying the actual benefits associated to BLI, such as the inlet flow distortion on engine efficiency, operability, aeromechanics and aeroacoustics. The fuselage boundary-layer ingestion, as well as the possible presence of a s-duct inlet, lead to the partial loss of the fan inflow axial uniformity, thus causing a strong azimuthal variation of the fan blade loading with aerodynamic and

aeroacoustic drawbacks. Therefore, this kind of engine integration deeply relies upon the possibility to alleviate the flow distortion and non-uniformity at the fan plane.

Although an extensive research has been conducted in order to investigate BLI propulsion systems in terms of performances and fuel efficiency [7,9–14], and inlet flow control analysis [15–17], the aeroacoustic assessment of BLI has not received much attention in the past and only few aeroacoustic studies are available in literature for such configurations.

Defoe et al. [18] have investigated the effects of BLI on the aeroacoustics of transonic fan rotors. They implemented a body-force formulation for the fan rotor description, extracted from a 3D Reynolds-Averaged Navier-Stokes (RANS) simulation, in an unsteady Euler calculation and evaluating the far-field noise via the Ffowcs-Williams & Hawkings (FW-H) integral method using a permeable surface. They found out that the dominant mechanism for changes in far-field rotor shock noise, due to the boundary-layer ingestion at low free-stream Mach numbers, is the ingestion of

stream-wise vorticity generated by the interaction of the upstream boundary-layer vorticity with the inlet lip.

A noise assessment at aircraft-level for the NASA D8 concept has been carried out by Clark et al. [19] by using the Aircraft Noise Prediction Program (ANOPP) comprehensive tool to predict the noise generated by each source component, with the BLI influence on fan noise empirically modeled based on experimental data. In that study, boundary-layer ingestion was predicted to have a detrimental impact on effective perceived noise levels in the order of 15 EPNdB.

Finally, Murray et al. [20] conducted aeroacoustic measurements for an unshrouded rotor partially immersed in a turbulent boundary-layer at low Mach number to investigate inflow distortion effects associated to airframe-integrated engines. They found out that, at low and moderate thrust conditions, the rotor produces broadband noise organized into haystacks generated by large eddies in the ingested turbulence being cut multiple times by neighboring rotor blades, contrarily to louder and more tonal acoustic signatures observed at high thrust conditions.

1.3. Scope of the present work

In view of the above, the existing research on fan BLI aeroacoustics is limited only to experimental/numerical studies at component level and to the analysis of BLI full-aircraft configuration by means of low-fidelity comprehensive codes. Since there are no detailed studies on the physics behind the noise generation for BLI embedded engines at full-aircraft level, the aim of this paper is twofold: (i) to perform the first, to the authors' knowledge, high-fidelity CFD/CAA simulation of a full-scale aircraft geometry comprehensive of a BLI fan/Outlet Guide Vane (OGV) stage; and (ii) to address BLI installation effects on fan noise for the NOVA BLI aircraft configuration by comparison between the same engine used in a conventional non-BLI and BLI layout. The analysis is carried out for an operating condition representative of a flyover with power cut-back to replicate one of the required conditions for noise certification [21].

In this paper, Simulia PowerFLOW® time-explicit, compressible and transient solver based on the lattice-Boltzmann Method/Very Large Eddy Simulation (LBM/VLES) is used to simulate and analyze the flow and the acoustic near-field around the BLI fan-stage configuration. The aerodynamic noise generated by the fan and its interaction with the ingested turbulence, as well as the fan wake/OGV interaction is then estimated by using an acoustic analogy based on Farassat's formulation 1A of the FW-H equation applied on a permeable surface encompassing the engine and part of the fuselage. This hybrid CFD/CAA methodology has been extensively used and validated in the past by several authors in a variety of experimental benchmark, ranging from airfoil trailing-edge noise [22] and jet noise [23] to rotorcraft [24,25] and aircraft aeroacoustics, both at component [26,27] and full aircraft level [28, 29]. More specifically, the same computational methodology has been successfully validated by Casalino et al. [30] and Gonzalez-Martino and Casalino [31] in the field on turbofan aeroacoustics. They predicted tonal and broadband noise of three fan/OGV configurations of the 22-in NASA Source Diagnostic Test (SDT) fan rig [32] with an accuracy in the order of the experimental uncertainty of 1 dB, at both subsonic and transonic tip speed conditions.

The manuscript is organized as follows. In Sec. 2, an overview of the LBM/VLES approach, far-field noise and on-the-ground noise computation are presented. The geometries and the computational setup used in this study are described in Sec. 3. Aerodynamic and aeroacoustic installation effects associated to the NOVA BLI configuration are discussed in Sec. 4. Finally, the main conclusions and future outlook of this study are drawn in Sec. 5.

2. Numerical method

2.1. LBM/VLES flow solver

The CFD/CAA solver Simulia PowerFLOW® is used in this study to compute the unsteady flow. The solver is based on the lattice-Boltzmann Method with a wall-modeled VLES approach for turbulence [33–36] and it solves the Boltzmann equation for the distribution function $g(\mathbf{x}, t, \mathbf{v})$ on a hexahedral mesh automatically generated around bodies. The function g represents the probability to find, in the elementary volume $d\mathbf{x}$ around \mathbf{x} and in the infinitesimal time interval $(t, t + dt)$, a number of fluid particles with velocity in the interval $(\mathbf{v}, \mathbf{v} + d\mathbf{v})$. The Boltzmann equation is solved by discretizing the space velocity domain into a prescribed number of values in magnitude and direction. These discrete velocity vectors are such that, in a prescribed time step, one particle can be advected from one point of the mesh to N neighboring points. In this study, a hybrid formulation of the solver is used, which allows to combine 19 (D3Q19) and 39 (D3Q39) particle velocity states, the latter being used where transonic flow is expected [37].

The standard LBM formulation is based on the time-explicit advection equation:

$$g_j(\mathbf{x} + \mathbf{v}_j \Delta t, t + \Delta t) - g_j(\mathbf{x}, t) = C_j(\mathbf{x}, t), \quad (1)$$

where g_j represents the particle distribution function along the j -th direction, according to the finite set of discrete velocities, and $\mathbf{v}_j \Delta t$ and Δt are the space and time increments, respectively. The left-hand side of the previous equation corresponds to the particle advection, while the right-hand side is the collision operator, which represents the rate of change of g_j resulting from collision (i.e. the interaction of particles). The collision term C_j is modeled with the Bhatnagar-Gross-Krook (BGK) approximation [38,39]:

$$C_j(\mathbf{x}, t) = -\Delta t / \tau [g_j(\mathbf{x}, t) - g_j^{eq}(\mathbf{x}, t)], \quad (2)$$

where τ is the relaxation time parameter, which is related to the fluid dimensionless kinematic viscosity and temperature, and g_j^{eq} is the equilibrium distribution function, which is related to local hydrodynamic properties [37]. For compressible flows, the LBM is coupled with an entropy partial differential equation to satisfy the conservation of energy (non isothermal model) [37]. Once the distribution function is computed, hydrodynamic flow quantities, such as flow density, velocity and internal energy, can be determined through discrete integration of the distribution function g_j [37]. All the other physical quantities can be determined through thermodynamic relationships for an ideal gas.

For simulations with a rotating geometry in time around a fixed axis, the computational domain is decomposed into an outer "ground-fixed" reference frame and an inner "body-fixed" Local Reference Frame (LRF). The latter domain is characterized by a grid which rigidly rotates with the rotating geometry in such a way that no relative motion between the LRF grid and the enclosed geometry occurs. Outside the LRF the fluid flow is solved using Eq. (1), whereas a modified version of Eq. (1), which includes an external body force term corresponding to the inertial force introduced by the non-inertial rotating LRF [40], is used inside it. A closed transparent interface is used between the inner and the outer domain in order to connect the two fluid flow regions [41].

The LBM scheme is solved on a grid composed of cubic volumetric elements (Voxels), the lattice, which is automatically created by the code. Different Variable Resolution (VR) regions are specified by the user to increase the discretization effort in regions of interest or in regions where high flow gradients are expected. A variable grid resolution by a factor of two is allowed between adjacent VRs. The solver uses an explicit time-marching scheme based

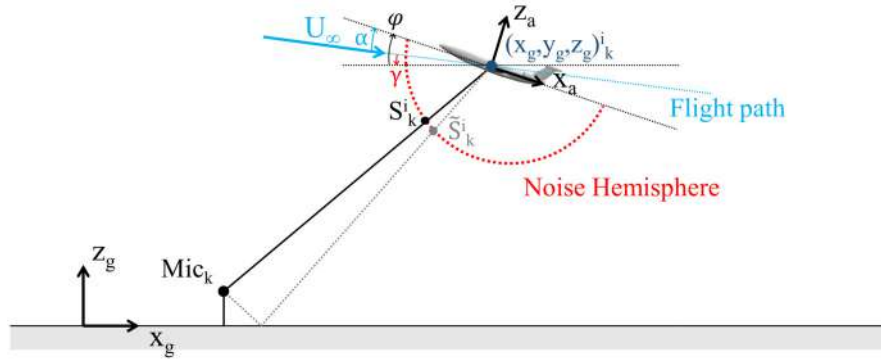


Fig. 1. Sketch of the on-the-ground EPNL footprint calculation procedure. α , γ and φ denote the aircraft angle of attack, glide angle and pitch angle, respectively.

on a unitary Courant-Friedrichs-Lewy (CFL) condition. Hence, the time step is also varied by a factor of two between adjacent VRs, and the solution in coarser VRs is updated at a lower rate compared to finer VRs. Thus, a balanced domain decomposition based on the equivalent number of voxels updated at every time step, i.e. the number of Fine Equivalent Voxel (FEV), allows a speed-up of the transient flow simulation. The surface of solid bodies is automatically facetized within each voxel intersecting the wall geometry using planar surface elements (Surfels). For the no-slip and slip wall boundary conditions at each of these elements, a boundary scheme [42] is implemented, based on a particle bounce-back process and a specular reflection process, respectively. Therefore, very complex arbitrary geometries can be treated automatically by the LBM solver, simplifying the tedious manual work typically associated with the volume meshing step using other CFD approaches.

2.2. Far-field noise computation

The CAA properties of LBM allow to analyze the acoustic near-field directly extracted from the transient flow solution. Due to the fact that the LBM is compressible and provides an unsteady flow solution, along with its low dissipation and dispersion properties [43], it is intrinsically suited for aeroacoustic simulations and allows to extract the sound pressure field directly in the near-field. In this study, a hybrid direct noise/FW-H acoustic analogy approach is adopted to compute the far-field noise while avoiding expensive computations associated to the necessity of accurately resolve the acoustic waves propagation up to the far-field.

The FW-H code used in this work is part the post-processing software Simulia PowerACOUSTICS[®], which is also used to perform statistical and spectral analysis of any unsteady solution generated by the CFD/CAA solver PowerFLOW[®]. Specifically, the employed FW-H solver [44] is based on a forward-time solution [45] of Farassat's formulation 1A [46] extended to a permeable (porous) integration surface. Such a formulation involves two surface integrals, referred to as thickness (monopole) and loading (dipole) terms, and neglects the volume integral (quadrupole term), which accounts for all the non-linear effects in the volume outside the integration surface. However, by using a permeable surface encompassing the fan-stage and part of the fuselage, it is possible to retrieve, by means of the monopole and dipole terms, all the noise sources and non-linearities included inside the integration surface itself (i.e. shock waves, turbulence mixing and propagation effects).

It is worth mentioning that the necessity to accurately capture the near-field noise propagation from the source region up to the FW-H integration surface is a requirement that can take advantage of the intrinsic low-dissipation and low-dispersion properties of the LBM scheme compared to partial differential equation discretization schemes.

2.3. EPNL computation

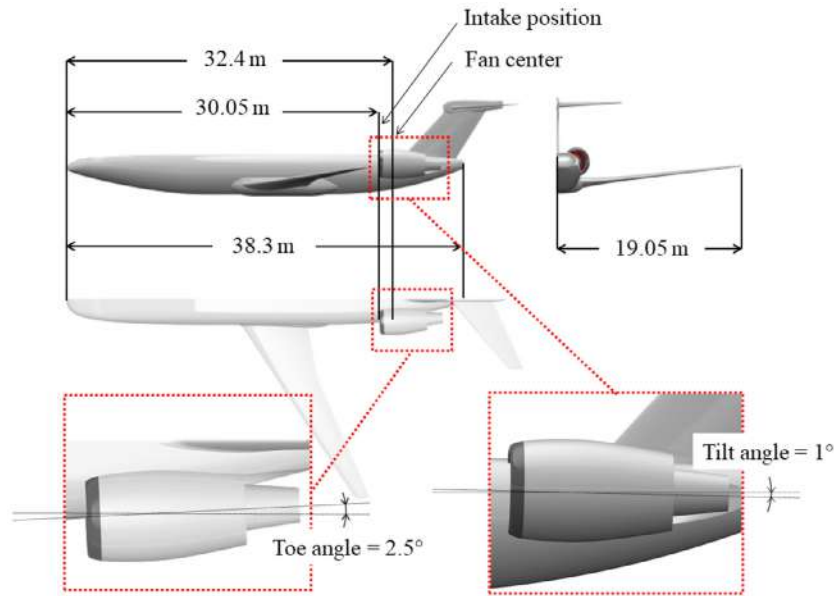
A computational procedure based on pre-computed LBM/FW-H acoustic signals is used in this work in order to compute the Effective Perceived Noise Level (EPNL) on the ground according to the FAR Part 36 procedure [21]. Mathematical details on the EPNL tool and its validation can be found in Casalino et al. [47]. For the sake of conciseness, only a brief overview of the procedure is outlined in the following. First, the permeable FW-H approach is used to compute the far-field noise signals and, in turn, Narrow-Band Noise (NBN) spectra (in the frequency range 50 Hz–10 kHz) on 300 microphones distributed over a hemisphere of 60 m radius. Such a hemisphere is centered around the aircraft reference frame (denoted by x_a , y_a and z_a) and is rigidly connected to the frame, as sketched in Fig. 1.

Then, for each microphone k on a ground carpet, and for every flight sub-segment i of 0.5 sec duration, the emission position $(x_g, y_g, z_g)_k^i$ of the aircraft is determined (with x_g , y_g and z_g being the ground-fixed, i.e. inertial, reference frame coordinates). A ray is traced between the microphone k and the vehicle emission position, and its intersection S_k^i with the rotated hemisphere determines the point where the NBN spectra are interpolated from the closest microphones on the hemisphere. Similarly, the intersection \tilde{S}_k^i between the reflected ray and the hemisphere is also determined, and the NBN spectra are interpolated at this point to account for ground reflection. Finally, the interpolated NBN spectra are projected on the ground carpet by applying spherical spreading, atmospheric absorption, Doppler effects, amplitude correction and ground reflection.

3. Fan-stage configurations and computational setup

3.1. Geometries and operating conditions

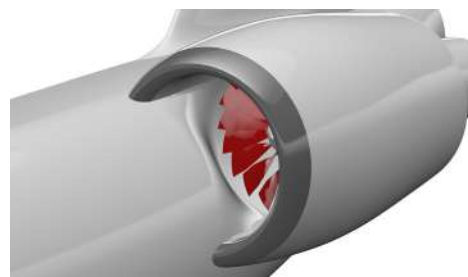
The geometry considered in this study is the NOVA lifting fuselage, wing and empennage (without engine and s-duct) - courtesy of ONERA - with a total length of 44 m and a semi-span of about 19 m. A modified version of the Low-Noise configuration of the NASA SDT, an existing scaled fan-stage configuration publicly available in the framework of the AIAA Fan Broadband Noise Prediction Workshop [32], was integrated into the fuselage to reproduce the NOVA BLI layout, as sketched in Fig. 2(a). In particular, the original Low-Noise SDT configuration, consisting of a 22-bladed fan and 26 stator swept vanes, was firstly scaled by a factor of 3.88 to match the NOVA fan radius ($R = 1.075$ m) and equipped with a redesigned nacelle, obtained by increasing the original inlet axial length in order to match the NOVA BLI engine intake-fan distance (2.35 m). A sketch of the modified Low-Noise SDT engine is depicted in Fig. 2(b). This redesigned engine geometry was then installed into the NOVA fuselage by considering a 40% buried intake,



(a) redesigned NOVA BLI aircraft configuration



(b) modified SDT fan-stage



(c) modified SDT fan-stage integration

Fig. 2. NOVA aircraft configuration equipped with the redesigned BLI engine nacelle.

as in the original NOVA BLI layout, and tilt and toe angles of 1° and 2.5° , respectively. Finally, a s-shaped duct was designed to integrate the fan-stage into the NOVA fuselage geometry, as shown in Fig. 2(c). This s-duct configuration turned out to be the best one in terms of inlet flow separation among three other different s-duct geometries, all based on the above mentioned design parameters and characterized by having tangent surfaces to the fuselage and nacelle walls. Since the primary goal of this study is to address the fan noise impact for the NOVA BLI layout, two different configurations are investigated: (i) the isolated SDT fan/OGV stage with the modified nacelle (Fig. 2(b)) and (ii) the installed SDT fan/OGV stage into the original NOVA fuselage geometry (Fig. 2(c)).

The operating conditions considered in this study are representative of a take-off with power cut-back, which represents one of the required conditions for noise certification. The free-stream Mach number is $M_\infty = 0.25$ and the static pressure ($p_\infty = 97718$ Pa) and temperature ($T_\infty = 286.15$ K) are taken from the International Standard Atmosphere (ISA) at 1000 ft. Moreover, the aircraft angle of attack is $\alpha = 4^\circ$, the pitch angle is $\varphi = 10^\circ$ and the glide angle is $\gamma = 6^\circ$ (note that the angle of attack is defined by the difference between the glide and pitch angles, i.e. $\alpha = \varphi - \gamma$). It should be pointed out here that such angles, which define the engine incidence with respect to the free-stream together with the tilt and toe angles, are also considered for the isolated engine configuration. Finally, the fan angular velocity is $\Omega = 2603$ RPM, corresponding to the 80% of SDT fan nominal power and re-

sulting into a tip Mach number and a Blade-Passing Frequency of $M_{tip} = 0.8680$ and $BPF = 954$ Hz, respectively.

3.2. Computational setup

Fig. 3 depicts some details of the computational setup and the grid adopted in this study. For the sake of conciseness, only those used for the BLI configuration are presented in the following. Identical setup and computational mesh, except for the presence of the fuselage geometry, are also used for the isolated configuration. The rotor and the spinner are encompassed by a volume of revolution that defines the LRF, i.e. the rotating sliding mesh region used to reproduce the fan rotation. Since no primary jet is considered in this study, the center-body geometry is extended by employing an infinite solid cylinder downstream with slip boundary conditions to avoid flow recirculation behind it. For the BLI configuration, a zig-zag strip of 3.5 cm height, 5.8 cm wavelength and 6.4 cm amplitude was placed 3R upstream the engine inlet in order to trigger transition and develop a fully turbulent boundary-layer at the fan-stage location, while keeping the computational effort relatively low. The FW-H integration surface (depicted in Fig. 3) used to compute the acoustic far-field consists of two regions: a spherical sector around the intake, and a conical surface in the exhaust region. The center part of the FW-H surface (cylinder) crosses through the solid walls of the nacelle: therefore, no flow data is extracted from there. The downstream cap of the cone

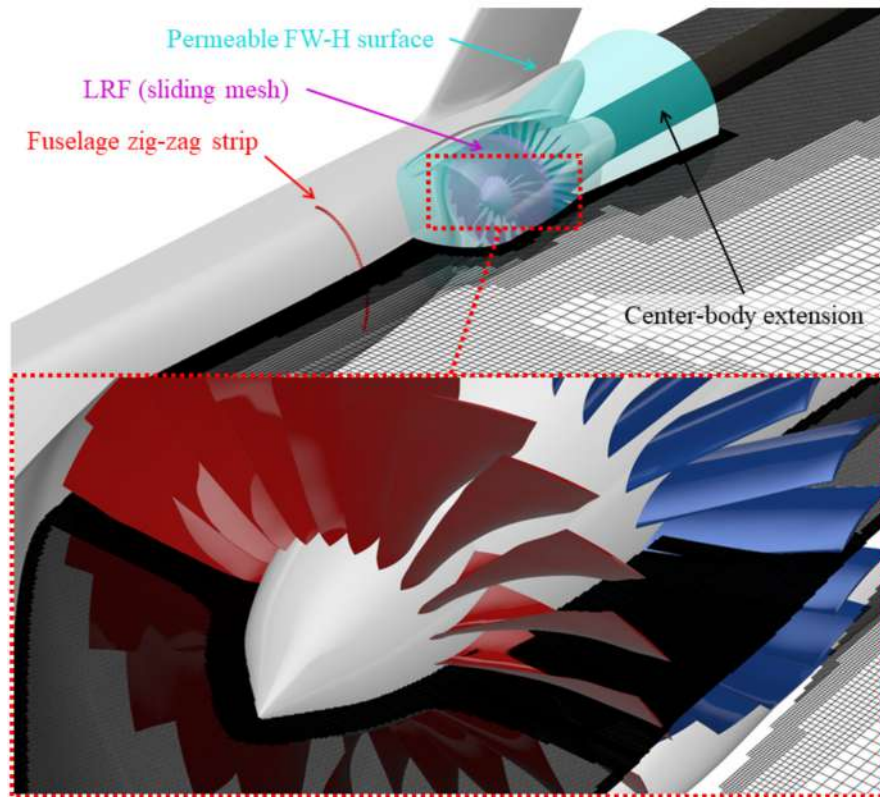


Fig. 3. Details of the computational setup around the fan-stage: LRF, fuselage transition trip, center-body extension and FW-H surface.

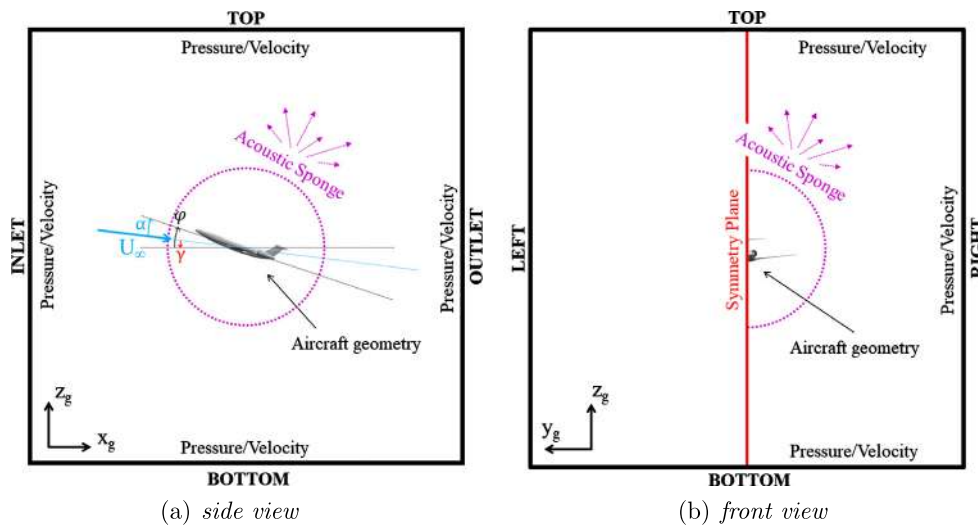


Fig. 4. Sketch of the computational domain: boundary conditions and acoustic sponge.

is not included, in order to avoid noise contamination due to the hydrodynamic pressure fluctuations in the wake of the fan. However, the FW-H cone extends downstream enough to recover the bypass exhaust radiation for the directivity angles of interest.

A cubic simulation volume of edge length of $690R$ centered around the engine is used. Free-stream static pressure and velocity are prescribed on the outer boundary, and an acoustic sponge approach is used to damp the out-going acoustic waves and minimize the backward reflection from the outer boundary (Fig. 4). The acoustic sponge is defined by two concentric spheres of radius $40R$ and $150R$, respectively, and centered around the engine geometry. Hence, the fluid kinematic viscosity is gradually increased starting from its real value within the inner sphere, up to an artificial value

two orders of magnitude higher outside the outer one. A symmetry plane located at the fuselage centerline is used to reduce the computational cost.

A total of 16 VR levels are employed to discretize the whole computational domain. The finest VR region covers the volume between the fan blade tip and the nacelle casing. The second finest VR level is used to discretize leading- and trailing-edges of both fan and OGV vanes. The third finest VR level is set as offset of the fan, the OGV and the nacelle bypass lip. The fourth finest VR level covers the whole bypass duct and the fuselage surface upstream the intake (for the BLI case). The fifth finest VR level encloses the permeable surface used for FW-H computations. Finally, all the other VRs, characterized by fuselage and/or engine offsets

Table 1

Grid size in millions of elements and computational cost.

Case	# Voxels	# FEVoxels	# Surfels	# FESurfels	kCPUh (10 revs)
Isolated engine	541.1	69.6	51.9	17.8	61.5
BLI engine	545.9	70.1	57.5	18.1	62.1

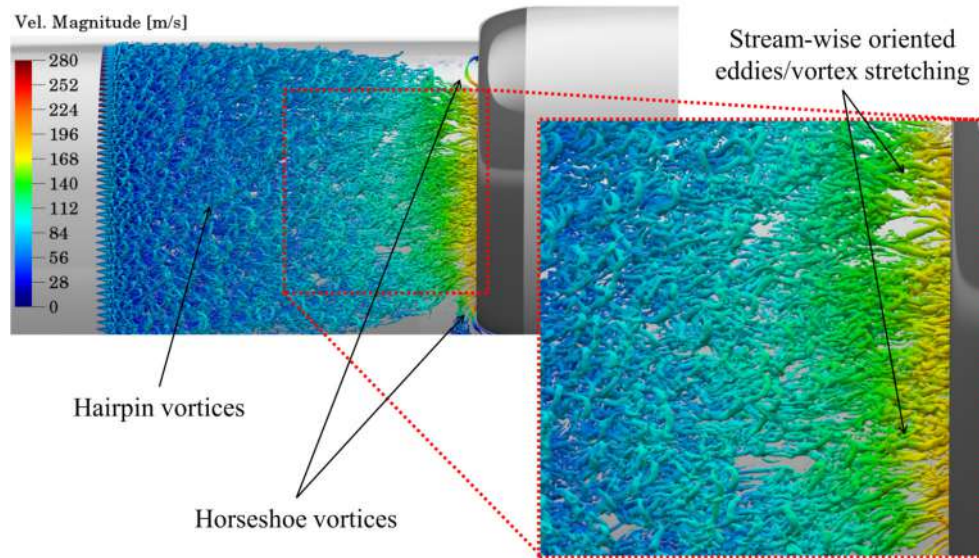


Fig. 5. Iso-surfaces of λ_2 (-75000 1/s^2) color-contoured by velocity magnitude depicting the turbulent boundary-layer past the transition trip. (For interpretation of the colors in the figure(s), the reader is referred to the web version of this article.)

and boxes, are used to model the remaining part of the computational domain up to its boundaries.

For the BLI configuration, a near-wall resolution which ensures a y^+ between 100 and 300 is prescribed on the fuselage surface in order to adequately capture the boundary-layer growth. Regarding the fan-stage region, the grid resolution employed in this study is based on the “fine” resolution successfully validated against the NASA SDT benchmark by Gonzalez-Martino and Casalino [31]. They demonstrated the capability of the solver to predict absolute broadband and tonal noise levels of the NASA SDT with an uncertainty of 1 dB, both at high-subsonic and transonic blade tip conditions. Such a resolution level results in a finest voxel size of 0.355 mm, roughly 6 voxels along the fan tip gap and 3.88 (i.e. the scaling factor) times coarser voxels for same VRs for the present computational setup. Due to this last aspect, the prediction of absolute broadband and tonal levels might be affected by an uncertainty larger than 1 dB. Nevertheless, the goal of the present study is to focus on BLI installation effects, and hence to highlight variations relative to the non-BLI configuration, rather than predicting absolute values.

Simulations are performed using a 1000 cores cluster with Intel Xeon CPU E5-2697 2.6 GHz and require approximately 6 hours per fan revolution for both isolated and BLI cases. A summary of the grid size and computational cost for both BLI and isolated cases are reported in Table 1.

The whole fluid domain is firstly initialized with a uniform stream-wise velocity corresponding to the free-stream conditions for a coarser simulation ($\sqrt{2}$ times coarser than the finer one), which is in turn used to initialize a finer resolution case. Hence, after a settling time of 2 fan revolutions, corresponding to 0.0461 sec of physical time, sampling is started. Acoustic data are sampled at 180 kHz along 10 fan revolutions (0.2305 sec). Fourier transformed data are evaluated using a bandwidth of 25 Hz, 50% window overlap coefficient and Hanning weighting.

4. Numerical results

In this section, the numerical results for both BLI and isolated fan-stage configurations are presented. First, an assessment of the turbulent boundary-layer being ingested by the engine for the installed case is presented. Then, BLI installation effects for the NOVA BLI configuration during a take-off with power cut-back are outlined in terms of fan-stage velocity field, fan performances, fan blade sectional airload, far-field noise directivity, noise power level and on-the-ground noise footprint.

4.1. Fuselage boundary-layer

As mentioned, a zig-zag transition trip is employed in this study to trigger transition of the fuselage boundary-layer being ingested by the fan-stage. According to Van der Velden et al. [48], who performed LBM-based Direct Numerical Simulations (DNS) of the flow past transition strips over flat plates, a canonical fully turbulent boundary-layer is experienced for a zig-zag strip after approximately 40 laminar boundary-layer thicknesses (evaluated at the location of the tripping device) downstream it. Following this study, and considering the actual laminar boundary-layer thickness evaluated at the transition trip location, a settling trip-engine distance of 1R would be required to ensure the ingestion of a fully turbulent boundary-layer into the fan-stage. Starting from these considerations, a larger and more conservative trip-engine distance of 3R was used.

An instantaneous view of iso-surfaces of λ_2 criterion [49] color-contoured by velocity magnitude is depicted in Fig. 5. This result qualitatively shows the presence of a turbulent boundary-layer convecting over the fuselage past the transition trip and being ingested by the fan-stage. Flow structures of coherence length proportional to the zig-zag strip are seen mixing and creating larger hairpins downstream it. Moreover, the stretch and re-orientation of the turbulent structures into stream-wise oriented filaments is

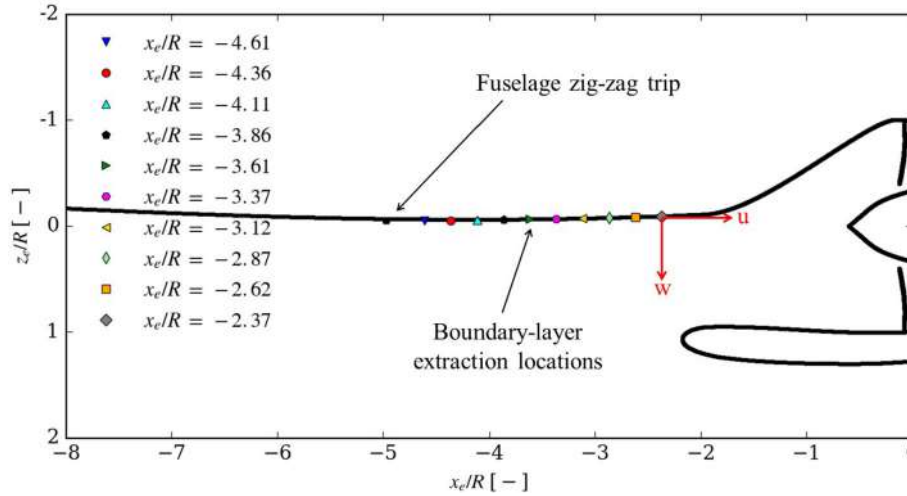


Fig. 6. Locations of the fuselage boundary-layer extraction and coordinate system for measuring the wall-parallel (u) and wall-normal (w) velocity components.

Table 2

Boundary-layer thickness δ and shape factor H at several locations between the zig-zag strip and the engine intake.

x_e/R [-]	-4.61	-4.36	-4.11	-3.86	-3.61	-3.37	-3.12	-2.87	-2.62	-2.37
δ [m]	0.1338	0.1522	0.1627	0.1702	0.1883	0.1842	0.1834	0.1929	0.1963	0.1993
H [-]	1.94	1.67	1.52	1.43	1.36	1.31	1.25	1.19	1.13	1.09

observed as the flow approaches the engine intake, as a result of the large flow acceleration occurring in proximity of the engine intake due to the favorable pressure gradient induced by the fan downstream. Finally, the generation of horseshoe vortices is further observed at the junction between the fuselage and the engine nacelle.

To better assess the presence of a turbulent boundary-layer being ingested by the fan-stage, boundary-layer profiles are extracted on the fuselage at 10 different equispaced locations between the zig-zag strip and the engine intake, as depicted in Fig. 6. Such locations are referred to the engine coordinate system (denoted by x_e , y_e and z_e coordinates), whose origin coincides with the fan center location, x -axis aligned with the engine axis and positive downstream, z -axis normal to the fuselage and directed outwards and y -axis defined by the right-hand rule. At each of these locations, time-averaged stream-wise velocity profiles \bar{u} (Fig. 7(a)), and time-averaged Reynolds stress profiles $\overline{u'u'}$, $\overline{w'w'}$ and $\overline{u'w'}$ (Fig. 7(b), Fig. 7(c) and Fig. 7(d), respectively) are extracted from the unsteady flow solution, where u and w represent the wall-parallel and wall-normal velocity components, respectively. In Figs. 7(a) to 7(d), the velocity statistics and the wall-normal distance are respectively normalized by the free-stream velocity $U_\infty = 88.78$ m/s and the local boundary-layer thickness δ (which is summarized for each location in Table 2 along with the shape factor H).

Moving from the zig-zag strip to the engine intake, the mean stream-wise velocity (Fig. 7(a)) shows an increment of the velocity gradient at the wall, with the transition from laminar-like to turbulent-like profiles already occurring for $x_e/R \leq -3.61$ (i.e. within roughly $1R$ distance from the tripping device). This is further confirmed by the shape factor H which goes below the threshold value of $1.3 - 1.4$ starting from $x_e/R \leq -3.61$, as expected for a turbulent boundary-layer [50]. Moreover, the outer parts of the different mean stream-wise velocity profiles tend to collapse on top of each other, with edge-velocity values slightly exceeding the free-stream one, for $x_e/R \leq -3.61$. Contrarily, the mean stream-wise velocity profiles show increasing edge-velocities at more downstream locations (up to approximately $1.75U_\infty$ for $x_e/R = -2.37$), as a consequence of the increasing favorable pressure gradient in the stream-wise direction. The

stream-wise (Fig. 7(b)), wall-normal (Fig. 7(c)) and shear (Fig. 7(d)) Reynolds stresses show a rapid reduction of the peak value within the first 5 stream-wise stations ($-4.61 \leq x_e/R \leq -3.61$), i.e. within $1R$ from the zig-zag strip, where the settling of the turbulence enforced by the zig-zag strip is expected [48]. For more downstream positions, a weaker reduction of the turbulent levels is further observed for the $\overline{u'u'}$ and $\overline{u'w'}$ components. Contrarily, the wall-normal component shows no reduction of the turbulent levels with converging profiles for locations close to the engine intake. This might be related to the stretching and re-orientation of the boundary-layer vortices in the stream-wise direction, with a consequent re-distribution of the turbulent kinetic energy from the $\overline{u'u'}$ to the $\overline{w'w'}$ components in the overall Reynolds stresses energy budget. Finally, it is interesting to point out that the Reynolds stress levels, extracted in proximity of the engine intake ($x_e/R = -2.37$), are consistent with those of a canonical developed turbulent boundary layer, whose values at a wall-normal distance of 0.2δ are approximately $\overline{u'u'}/U_\infty^2 = 4.5 \cdot 10^{-3}$, $\overline{w'w'}/U_\infty^2 = 1.6 \cdot 10^{-3}$ and $-\overline{u'w'}/U_\infty^2 = 1.3 \cdot 10^{-3}$ according to Klebanoff [51].

4.2. Fan-stage velocity field

Fig. 8 depicts a schematic description of a plane normal to the fuselage and passing through the engine axis, and different cross-flow planes along the inlet, interstage and bypass exhaust sections, which are used in the following to extract the fan-stage axial (i.e. aligned with engine axis) and in-plane (i.e. perpendicular to the engine axis) velocity fields along the engine. In this sketch, the x_e , y_e and z_e coordinates represent those of the engine coordinate system previously defined.

Fig. 9 shows the instantaneous axial velocity field for the BLI case extracted on a plane normal to the fuselage surface and passing through the engine axis at different time instants. The same quantity is depicted on the same plane for the isolated case in Fig. 10. The BLI configuration shows a flow acceleration at the intake section, due to the reduced inlet throat area of the installed configuration compared to the isolated one, and the presence of turbulence impinging the fan rotor. Such turbulent structures are connected to the fuselage turbulent boundary-layer being ingested

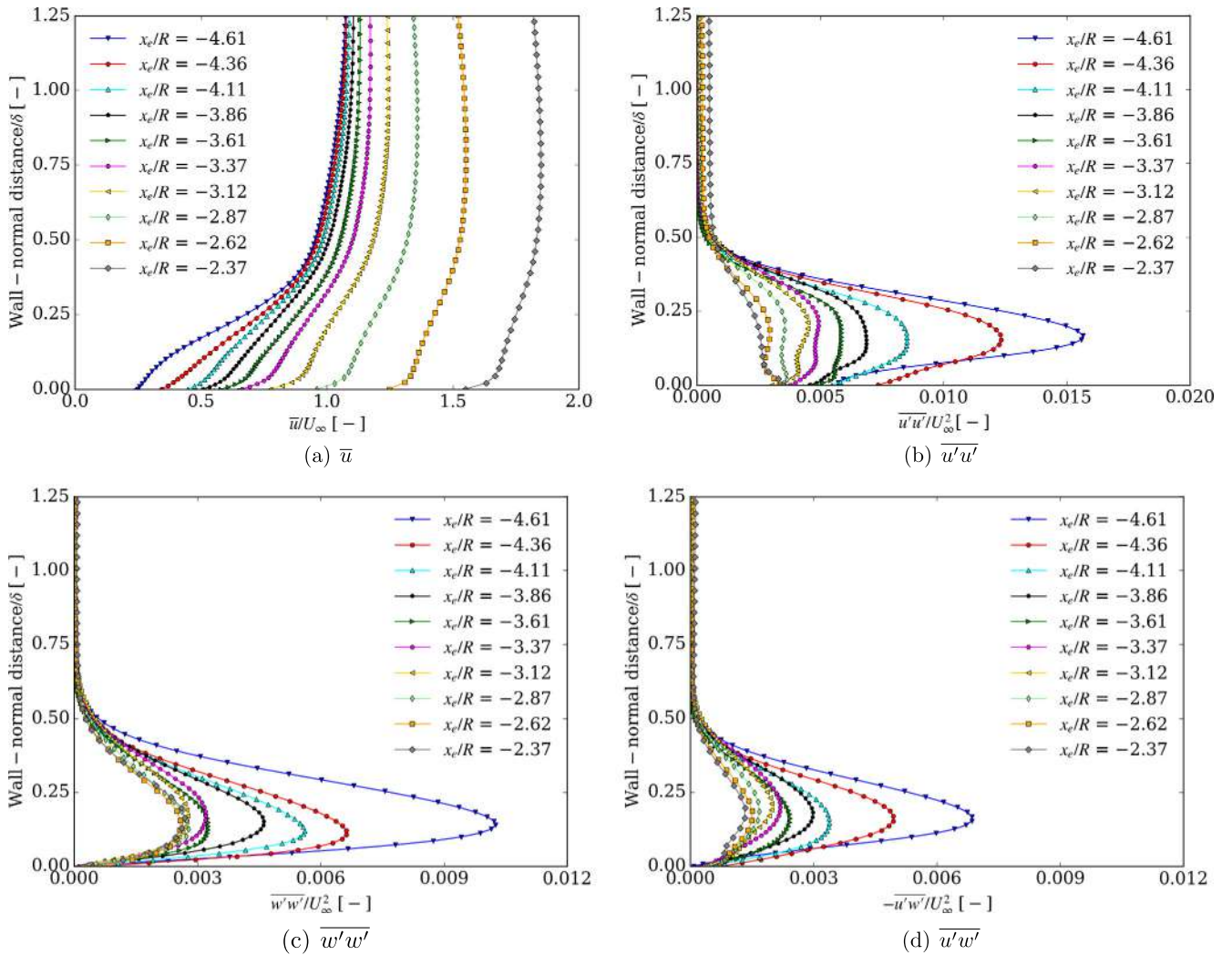


Fig. 7. Time-average stream-wise velocity (a) and Reynolds stress (b, c and d) profiles at several locations between the zig-zag strip and the engine intake.

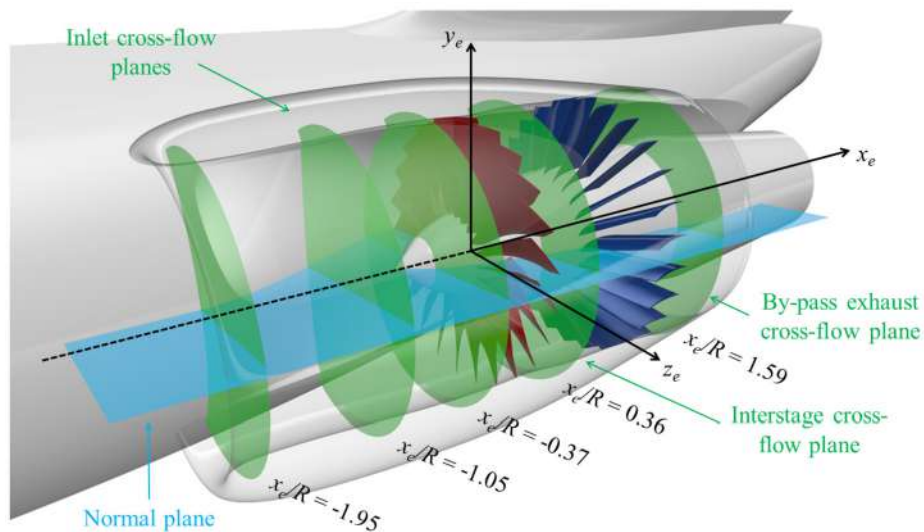


Fig. 8. Sketch of the planes used to extract the fan-stage velocity fields across the engine.

by the fan-stage, as well as to the flow separation occurring at approximately 60% of the s-duct length, the latter induced by the adverse pressure gradient due to the rapid increase of the intake cross-sectional area. Conversely, the isolated configuration shows

a rather uniform velocity field upstream the fan rotor, except for the first 25% of its extension, in which the flow tends to recover from its initial misalignment with the axis engine due to the presence of non-zero angle of attack, and tilt and toe angles. Upstream

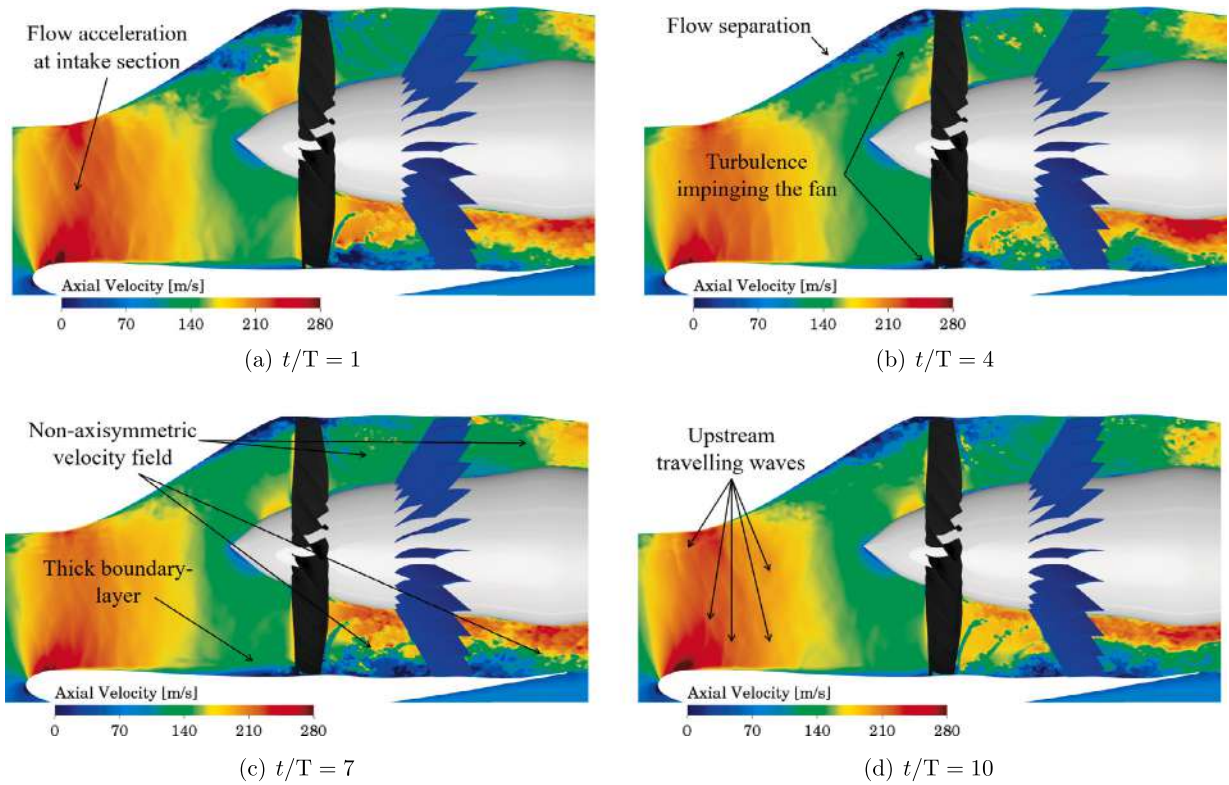


Fig. 9. Instantaneous axial velocity field on a plane normal to the fuselage surface and passing through the engine axis at different time instants, BLI engine.

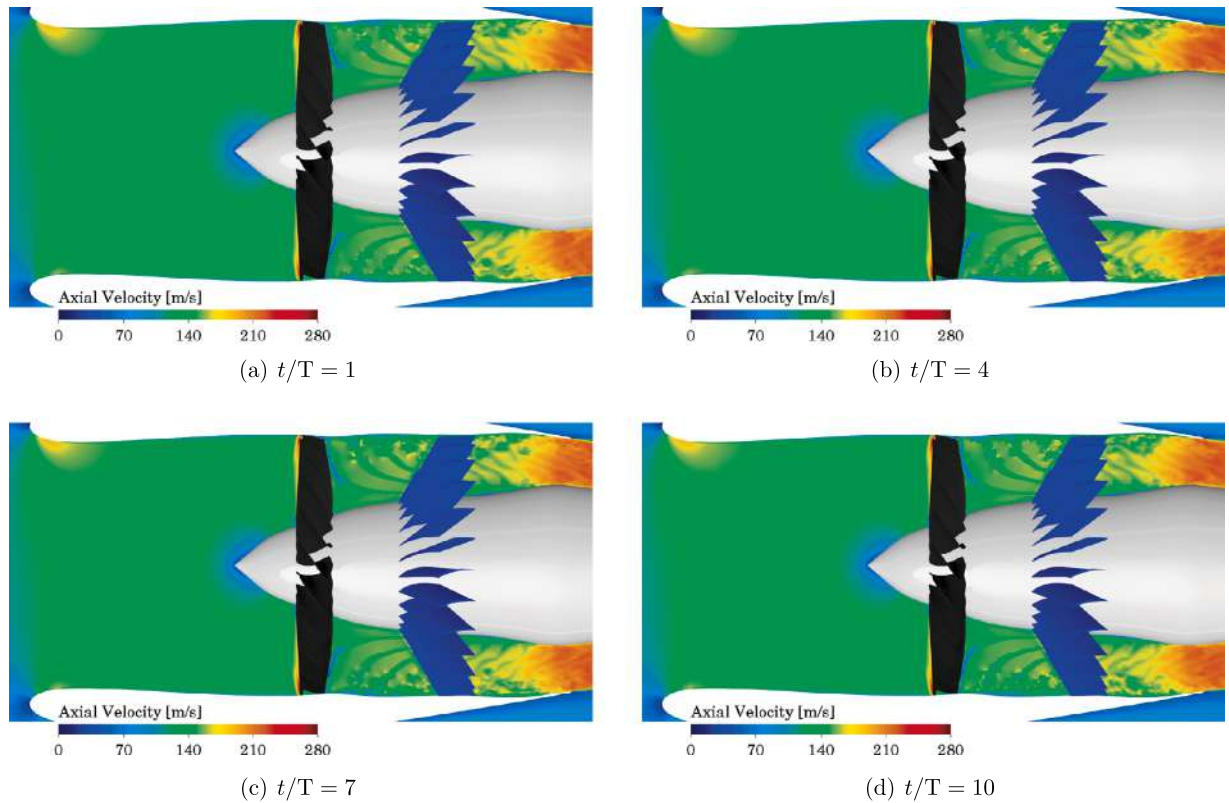


Fig. 10. Instantaneous axial velocity field on a plane normal to the fuselage surface and passing through the engine axis at different time instants, isolated engine.

traveling waves are observed along the intake for the BLI engine, unlike the isolated one. The BLI configuration shows a thicker boundary-layer on the intake wall opposite to the fuselage compared to the isolated case, which also tends to separate in prox-

imity of the wall beneath the fan. The instantaneous axial velocity field further shows the occurrence of two different fan wake/OGV interaction mechanisms between the fuselage and the nacelle sides for the BLI case, whereas the isolated case shows the typical rotor-

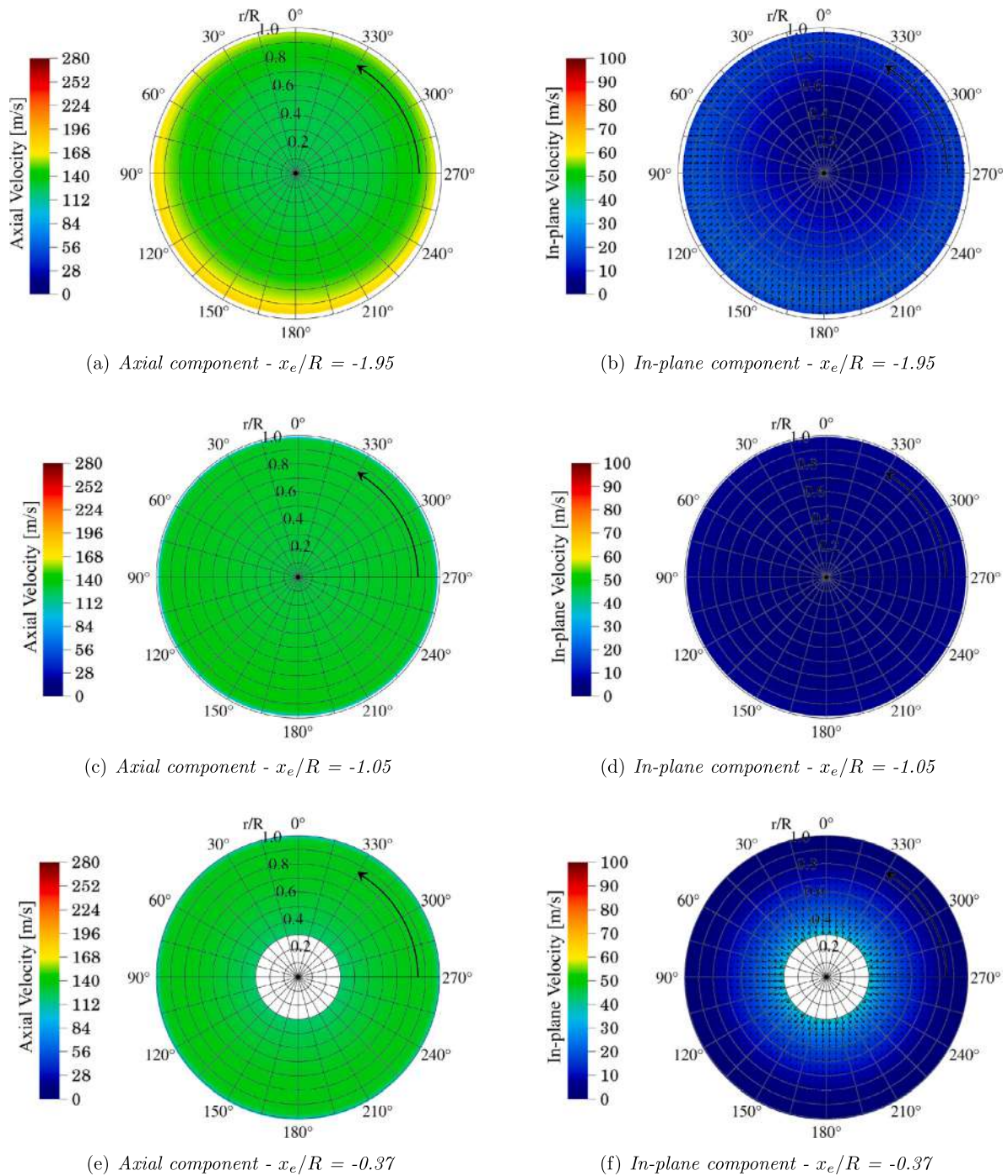


Fig. 11. Time-averaged velocity field at different sections upstream the fan, isolated engine.

stator interaction mechanism with the fan viscous wakes impinging on each stator vanes at the blade-passing frequency. The BLI configuration shows a non-axisymmetric velocity field between the rotor and the stator, with much higher velocities observed in the region opposite to the fuselage side with respect to the isolated one. In this same region, the BLI case further shows stronger turbulent structures than those convecting on the fuselage side. Similar considerations can be made for the fluid regions downstream the stator as well.

4.2.1. Inlet flow field

Figs. 11 and 12 show the time-averaged axial and in-plane velocity components on cross-flow disks upstream the fan plane for

the BLI and isolated configurations, respectively. For the in-plane velocity plots, the in-plane velocity vectors are also shown. In these upstream-looking-downstream views the fan blades rotate counter-clockwise as indicated by the black circular arrow. Three different stream-wise locations (i.e. $x_e/R = -1.95$, $x_e/R = -1.05$ and $x_e/R = -0.37$), respectively corresponding to 15%, 55% and 85% of the inlet axial length, are considered. Moreover, the convention adopted to describe the fan blade azimuth angle is also reported. According to this convention, the fan blade sweeps the BLI area for azimuthal angles between 45° and 180° (Fig. 12).

The isolated case shows a moderate level of distortion across the engine intake, where the free-stream misalignment with the engine axis (due to the non-zero angle of attack, and tilt and toe

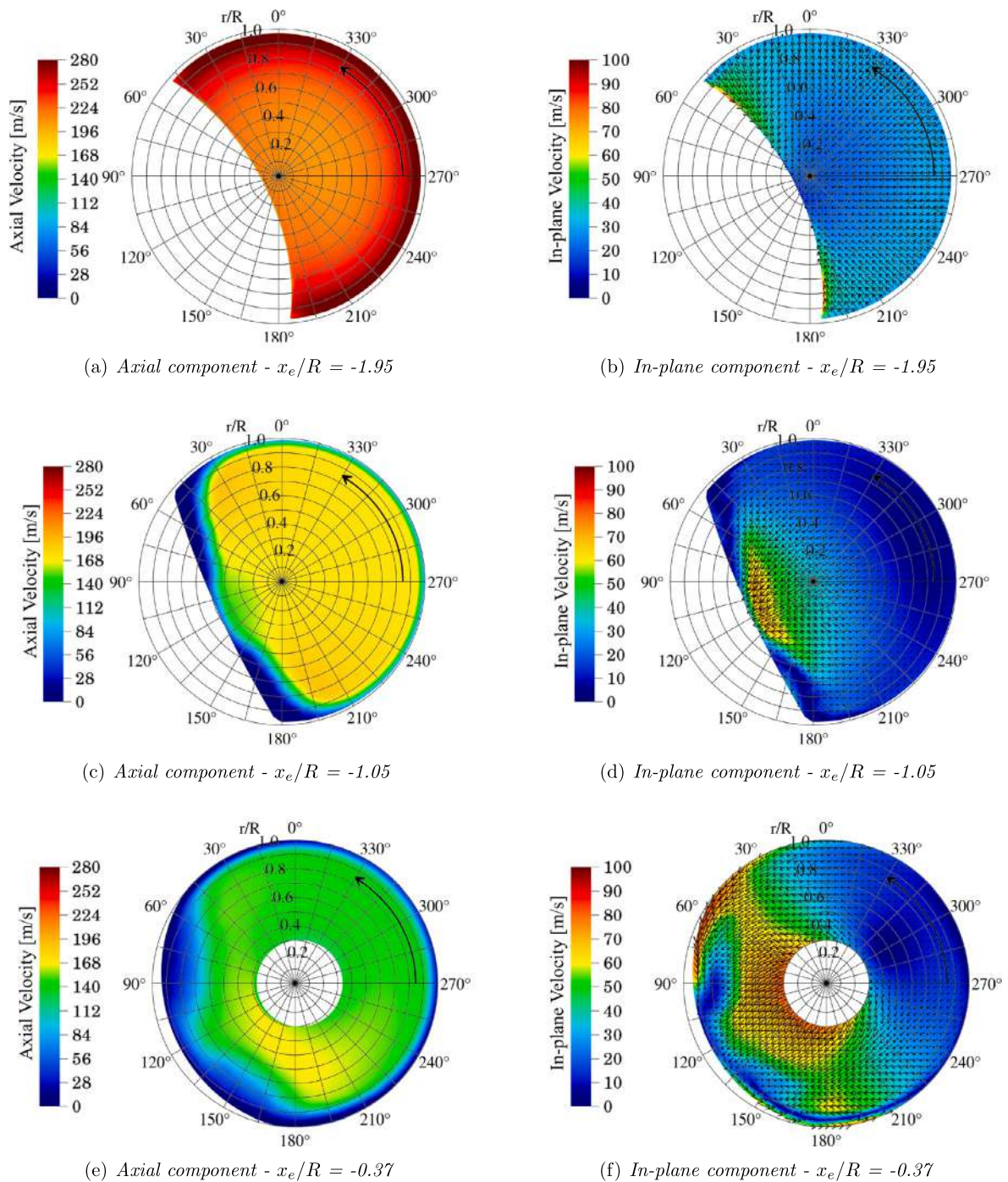


Fig. 12. Time-averaged velocity field at different sections upstream the fan, BLI engine.

angles) is responsible of the non-symmetric acceleration of the flow around the intake lip (Fig. 11(a)) and the arise of an in-plane velocity component directed inboard (Fig. 11(b)). The velocity field uniformity is then completely re-established within the first half of the intake extension, where the flow approaching the fan section shows a quite constant mean axial velocity (Figs. 11(c) and 11(e)) and a moderate in-plane velocity directed outwards along the radial direction, as a consequence of the slightly divergent inlet geometry (Fig. 11(d)) and the presence of the spinner downstream (Fig. 11(f)).

Regarding the BLI configuration, the reduced engine intake frontal area yields to an increase of the axial (Fig. 12(a)) and in-plane inward directed (Fig. 12(b)) velocity components com-

pared to the isolated case, the latter primarily showing a radial pattern with the highest magnitude values occurring around the junction between the fuselage and the engine nacelle. For further downstream sections, the mean flow exhibits high levels of non-uniformity and distortion in terms of both axial and in-plane velocities. More specifically, the axial component shows two nearly symmetric recirculation/low-velocity regions on the fuselage side. Such flow separation areas are already visible at 55% of the inlet length (Fig. 12(c)) and extend further downstream (Fig. 12(e)) according to a nearly symmetrical pattern around the inlet plane of symmetry (around 120° in the fan blade azimuth). A nearly symmetrical pattern around 120° of the fan blade azimuth is also observable for the in-plane velocity at $x_e/R = -1.05$ (Fig. 12(d)),

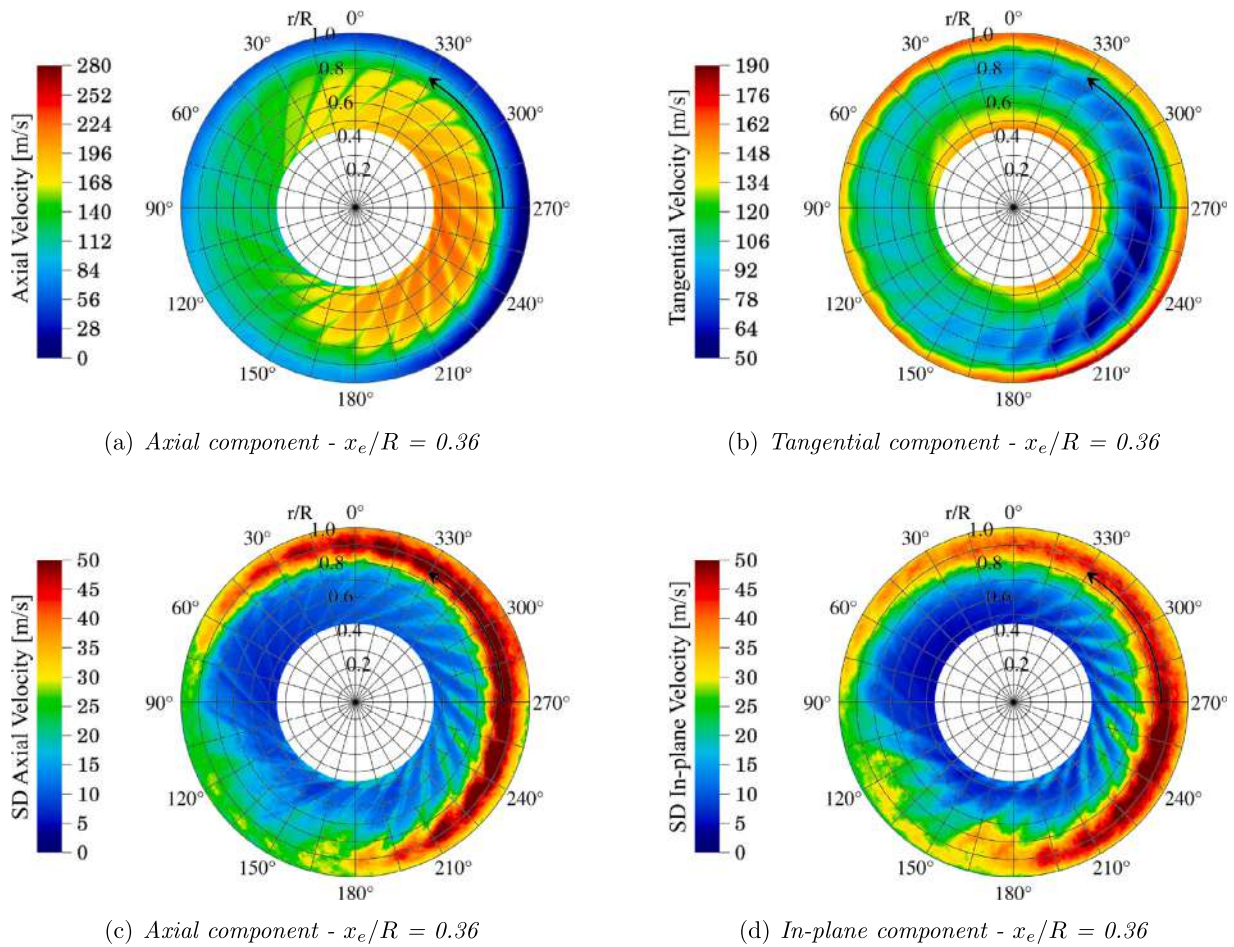


Fig. 13. Phase-locked average of axial (a) and tangential (b) velocity components and standard deviation (SD) of axial (c) and in-plane (d) velocity components on an interstage disk at $x_e/R = 0.36$, BLI engine.

which shows the presence of a strong secondary flow directed from the engine nacelle side towards the fuselage one, as a consequence of the centrifugal pressure gradient due to the s-duct geometric curvature. This transverse secondary flow is also observed for the inlet section at $x_e/R = -0.37$, which further shows an entrainment motion imparted by the rotor blades on the low-velocity flow approaching the fan face (Fig. 12(f)), i.e. for $r/R > 0.9$ and azimuthal angles within 45° - 90° and 135° - 210° , respectively.

It should be recalled that the current NOVA BLI configuration represents a rather idealized BLI-layout, due to the relative short s-duct length (2.35 m) and the large portion of intake embedded into the fuselage (40%). A more conservative sizing, e.g. based on a longer s-duct length and a lower percentage of buried intake, would help in reducing the amount of flow separation occurring on the s-duct, as well as of flow distortion at the fan plane. This at the cost of additional mass, drag and inlet friction losses.

4.2.2. Interstage flow field

Figs. 13 and 14 show upstream-looking-downstream views of the velocity field for an interstage section between the rotor and the stator ($x_e/R = 0.36$) for the BLI and isolated configurations, respectively. More specifically, the velocity field is decomposed into phase-locked average of axial (Figs. 13(a) and 14(a)) and tangential (Figs. 13(b) and 14(b)) velocity components, and standard deviation of axial (Figs. 13(c) and 14(c)) and in-plane (Figs. 13(d) and 14(d)) velocity components. It is worth mentioning that the phase-locked average contour plots highlight the presence of periodic non-uniformities in the mean flow associated to the rotating

fan blades (i.e. viscous blade wakes and tip-vortices), which generate tonal noise at BPF and its harmonics when they interact with the stator vanes. Instead, the phase-locked standard deviation contour plots can be used to examine the presence of random fluctuations in the flow (i.e. turbulence), which represent potential sources of broadband noise when they impinge on the stator surfaces.

Contrarily to the isolated configuration, where the two typical expected flow regions downstream the fan, i.e. the “viscous” region associated to both rotor blade wakes and tip-vortices and the “potential” flow region outside the viscous ones [52], are clearly defined throughout the radial coordinate (Figs. 14(a) and 14(b)), the same regions are visible only up to $r/R = 0.8$ of the span-wise coordinate for the BLI case (Figs. 13(a) and 13(b)). For the isolated configuration, the axial velocity in the potential flow regions is rather uniform (Fig. 14(a)) along the span-wise direction, whereas the tangential (Fig. 14(b)) ones tend to decrease for larger r/R . Moreover, for a given radial position, the axial velocity is lower in the viscous regions of the flow compared to the potential ones, whereas the tangential ones result to be higher. Similar trends can also be found for the BLI configuration, although some additional considerations need to be outlined. First, the phase-locked average axial velocity shows a non-uniform distribution along the azimuthal coordinate, with higher values within 0° - 45° and 135° - 360° and lower values in the complementary circular sector compared to the isolated case. The same trend also occurs for the tangential component within the first 55% of the radial coordinate, whereas an opposite situation is observed for $0.55 < r/R < 0.9$. Finally, the BLI configuration shows lower axial velocities and

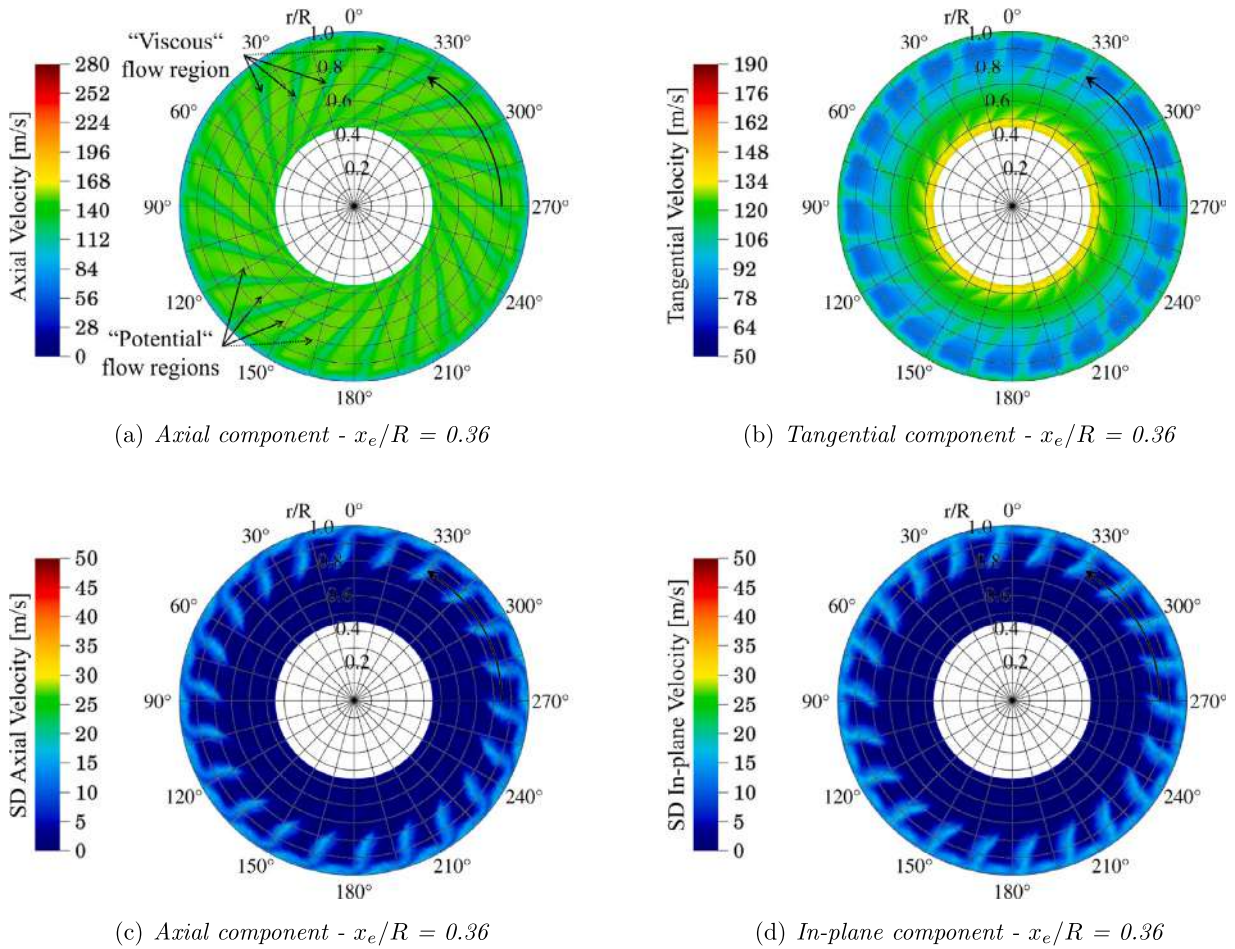


Fig. 14. Phase-locked average of axial (a) and tangential (b) velocity components and standard deviation (SD) of axial (c) and in-plane (d) velocity components on an interstage disk at $x_e/R = 0.36$, isolated engine.

higher tangential velocities above $r/R = 0.9$ compared to the isolated one. Regarding the turbulent fluctuations, the isolated case shows quite uniform standard deviation contours, with the largest velocity perturbations occurring within the viscous wake and at the tip for both axial (Fig. 14(c)) and in-plane velocity components (Fig. 14(d)). Contrarily, the BLI configuration shows larger levels of fluctuations and flow non-uniformity for both components (Figs. 13(c) and 13(d), respectively). More specifically, velocity fluctuations roughly three times higher are observed within the outer 30% of the radial coordinate and for azimuthal position comprised between 0° - 60° and 180° - 360° , respectively. A secondary diffused region of high turbulence levels is also present between 50° - 180° , i.e. in correspondence of the fuselage BLI area. Moreover, thicker viscous wakes are observed for the BLI configuration compared to the isolated one, especially for azimuthal angles between 180° and 360° .

Overall, the BLI interstage flow field is characterized by less axisymmetric and coherent tangential velocity variations and higher levels of in-plane velocity fluctuations. Such velocity components are thought to be more important in the generation of the rotor/stator interaction noise [52]. This type of noise is associated to the unsteady loading on the stator vanes, which is generated by fluctuations of the flow velocity component normal to the stator surface. In view of this, broadband noise is expected to dominate more the far-field noise spectrum for the BLI configuration compared to the isolated case. The detailed aeroacoustic analysis will be performed in Secs. 4.5 and 4.6 to proof the assumption.

4.2.3. Bypass exhaust flow field

To conclude the analysis of the fan-stage velocity field, Figs. 15 and 16 show upstream-looking-downstream views of the velocity field on a bypass exhaust transverse section ($x_e/R = 1.59$) for the BLI and isolated configurations, respectively. Again, the velocity field is presented in terms of phase-locked average of axial (Figs. 15(a) and 16(a)) and tangential (Figs. 15(b) and 16(b)) velocity components, and standard deviation of axial (Figs. 15(c) and 16(c)) and in-plane (Figs. 15(d) and 16(d)) velocity components.

As already pointed out, the BLI case shows a non-axisymmetric phase-locked average axial velocity field along the azimuthal coordinate downstream the stator (Fig. 16(a)), with the highest and lowest values respectively taking place on the nacelle side up to $r/R = 0.7$ and above $r/R = 0.9$. Contrarily, the isolated configuration presents the expected axisymmetric axial velocity pattern characterized by the viscous wakes being convected from each stator vane (Fig. 16(a)). The BLI configuration further shows a non-uniform and lower flow swirl recovery downstream the stator (Fig. 15(b)) compared to the isolated one (Fig. 16(b)), with high values of the tangential velocity still persisting along most of the outer part of the bypass exhaust ($r/R > 0.9$) and for the azimuthal sector between 225° and 315° . Concerning the turbulence levels in the bypass exhaust, the isolated case shows again quite axisymmetric standard deviation contours, with the largest velocity fluctuations occurring above 80% of the radial coordinate for both the axial (Fig. 16(c)) and in-plane (Fig. 16(d)) velocity components. Finally, similarly to what observed for the interstage velocity field,

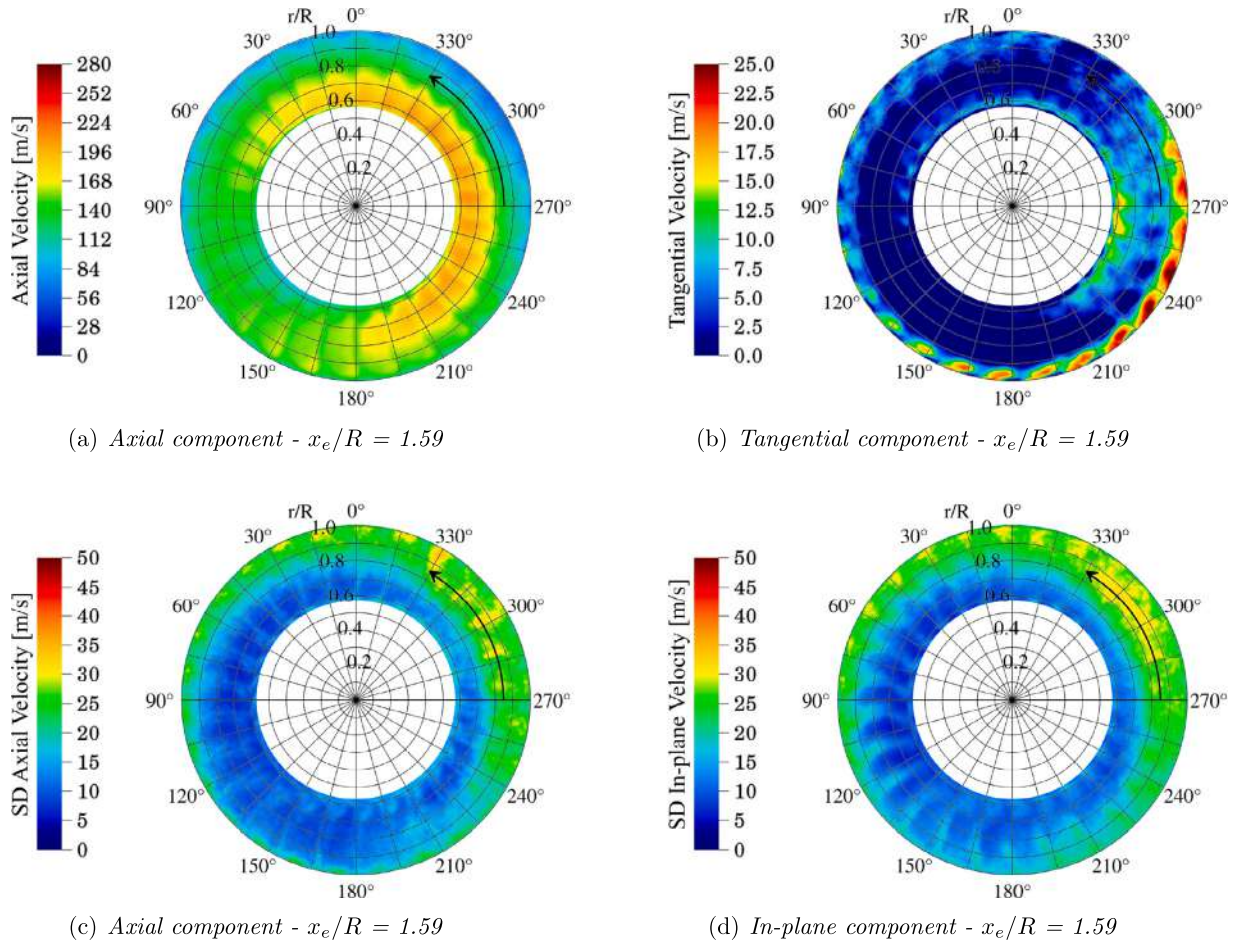


Fig. 15. Phase-locked average of axial (a) and tangential (b) velocity components and standard deviation (SD) of axial (c) and in-plane (d) velocity components on a disk in the bypass exhaust at $x_e/R = 1.59$, BLI engine.

Table 3

Fan pressure ratio, fan isentropic efficiency and relative difference between isolated and BLI engines.

Parameter	Isolated engine	BLI engine	Relative difference
FPR [-]	1.27	1.24	-2.5%
η_f [-]	0.917	0.836	-9.2%

the BLI configuration manifests large values of velocity fluctuations for both the axial and in-plane components (Figs. 15(c) and 15(d), respectively), with levels approximately three times higher than those of the isolated case for $r/R > 0.7$ and for the azimuthal sectors within 0° - 60° and 180° - 360° .

4.3. Fan performances

Table 3 shows BLI installation effects on the fan performances in terms of fan pressure ratio FPR and isentropic efficiency η_f . As a consequence of the highly distorted flow and the ingestion of turbulence, a reduction the FPR by 2.5% and of the isentropic efficiency by 9.2% is observed when the same fan is operated at same RPM in the BLI layout with respect to the conventional non-BLI case.

4.4. Fan blade section airload

Fig. 17 depicts the sectional thrust coefficient time-history $c_T \tilde{V}^2$ at 6 different span-wise sections uniformly distributed between 45% and 95% of the blade span. For each section and fan

blade azimuthal position, the $c_T \tilde{V}^2$ coefficient is computed by integration of the airfoil pressure distribution p over the airfoil contour Σ using the following formula:

$$c_T \tilde{V}^2 = - \frac{\oint_{\Sigma} p \mathbf{n} \cdot \mathbf{i}_{x_e} d\Sigma}{\frac{1}{2} \rho_{\infty} V^2 \ell_c} \tilde{V}^2 = - \frac{2}{\rho_{\infty} a_{\infty}^2 \ell_c} \oint_{\Sigma} p \mathbf{n} \cdot \mathbf{i}_{x_e} d\Sigma \quad (3)$$

where \mathbf{n} is the outward-pointing normal to the airfoil contour, \mathbf{i}_{x_e} is the engine axis unit vector (positive when directed downstream) and $d\Sigma$ is the infinitesimal airfoil contour element. Moreover, $\tilde{V} = V/a_{\infty}$ is the fan blade sectional velocity ($V = \Omega r$) at the radial coordinate r normalized by the free-stream speed of sound a_{∞} , ρ_{∞} is the free-stream density and ℓ_c is the airfoil chord. Note that the line integral in Eq. (3) is computed clockwise with respect to the airfoil contour Σ . As expected, the isolated configuration shows almost constant time-histories of the sectional thrust for each span-wise location, with a mean value increment moving from inboard (Fig. 17(a)) to outboard (Fig. 17(f)) sections of the fan blade. Only the outer section at $r/R = 0.95$ shows some weak unsteadiness due to the interaction between the blade tip and the boundary-layer developing along the inlet wall. Contrarily, the BLI configuration shows a low-frequency thrust unsteadiness (predominantly 1/rev) for inboard blade sections (Figs. 17(a) to 17(c)), as a consequence of the strong mean flow distortion. For these sections, an increment of the sectional thrust is observed approximately between 60° and 180° (i.e. in correspondence of the BLI area) compared to the isolated case, whereas lower values of

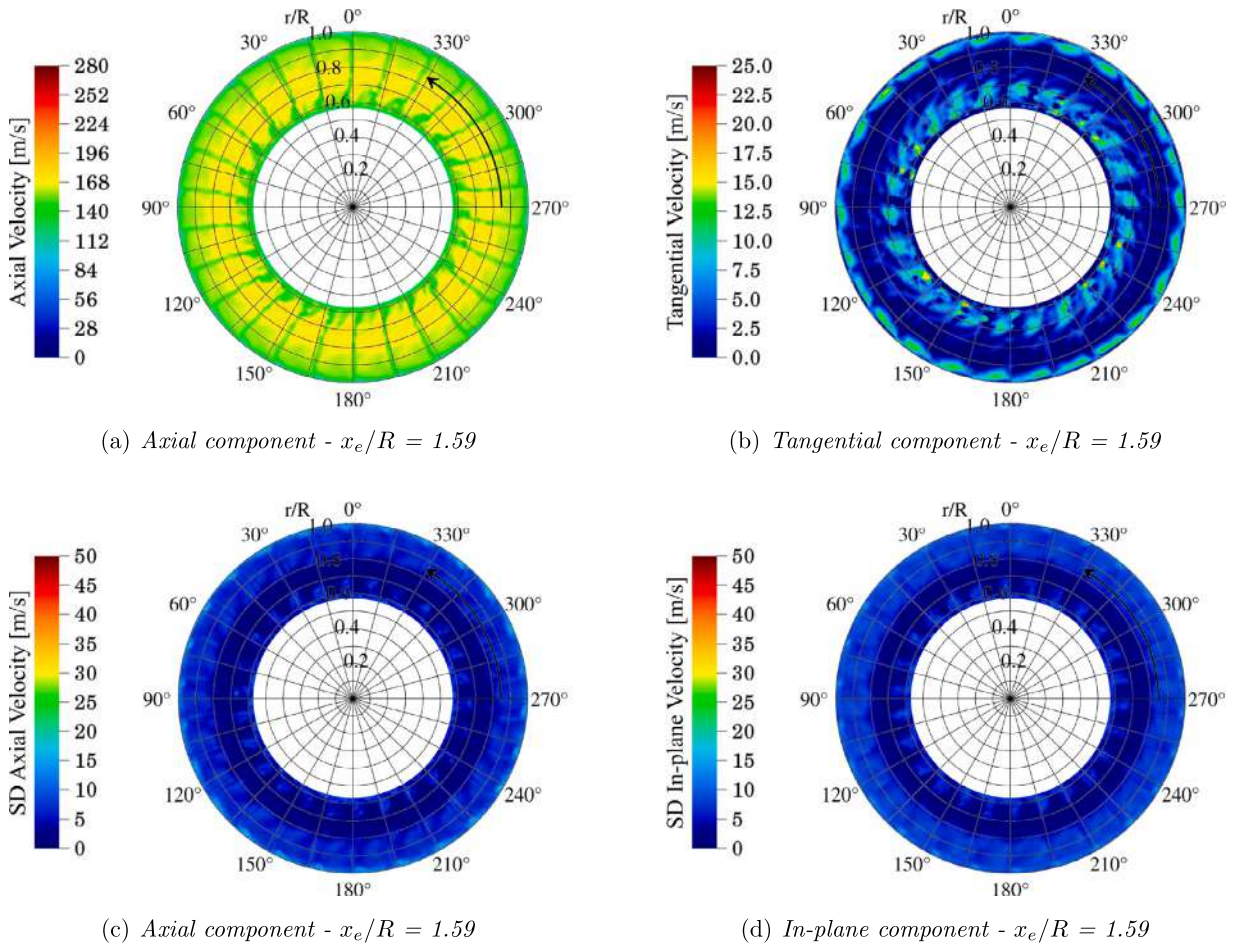


Fig. 16. Phase-locked average of axial (a) and tangential (b) velocity components and standard deviation (SD) of axial (c) and in-plane (d) velocity components on a disk in the bypass exhaust at $x_e/R = 1.59$, isolated engine.

the $c_T \bar{V}^2$ coefficient are observed elsewhere. As the radial coordinate increases, more intense and impulsive unsteadiness, as well as lower mean values of the sectional thrust are observed (Figs. 17(d) to 17(f)) compared to the isolated case, due to the ingestion of turbulence associated to the flow separation occurring on the nacelle and fuselage sides, respectively.

All the aforementioned thrust fluctuations represent an additional source of noise. Among them, those occurring on the outer part of the blade are expected to contribute more to the far-field noise, due to the higher levels of unsteadiness and Mach numbers compared to those in blade inboard regions.

4.5. Far-field noise directivity

Fig. 18 depicts the microphone array used in this study for far-field noise computations. It is composed by 7 even meridian arcs of 10 m radius, centered around the fan center and covering a semi-spherical surface. Each arc is characterized by 15 microphones distributed every 10° , with directivity angles ranging from 20° upstream the engine to 160° downstream it.

As mentioned in Sec. 3.2, the far-field noise is computed by integration of the FW-H equation on a permeable surface encompassing the engine. Since the FW-H formulation adopted in this work does not include the volume integral, spurious signals might arise when the permeable surface is intersected by turbulence (i.e. the fuselage turbulent boundary-layer) [53]. The presence of such spurious effects has been assessed (for the BLI case) by comparing far-field noise predictions from the whole permeable FW-H surface

to those obtained by removing that portion of the surface intersected by the fuselage boundary-layer. It turned out that the two different approaches provided almost identical results within the directivity angles of interest, thus allowing the use of the whole FW-H permeable surface (even for the BLI configuration) for the far-field noise computations.

A spectral representation (Power Spectral Density, PSD) of the far-field noise directivity normalized by the BPF is shown in Fig. 19 and Fig. 20 for the BLI and isolated cases, respectively. In addition, far-field noise differences between such configurations are depicted in Fig. 21. For the sake of conciseness, only the results for the arcs at $\phi = 0^\circ$ (ground arc) and $\phi = 90^\circ$ (sideline arc) are shown in following. For both the BLI and isolated configurations, the noise is radiated most efficiently downstream the engine. However, besides such a similarity, the two examined configurations show quite different results. The isolated engine presents both broadband and tonal noise contributions, with the latter showing distinct peaks at multiples of the blade-passing frequency downstream the engine (up to BPF-3). Conversely, tones at harmonics of the BPF do not emerge with respect to broadband levels for the BLI case. Haystacked peaks are found around BPF-1 for downstream directivity angles, as better highlighted in Fig. 22 for the ground arc at 140° and 150° observer angles. Such peaks are believed to be generated by the correlated unsteady airloads on neighboring blades, and associated to both the stream-wise elongated vortices coming from the fuselage turbulent boundary-layer and the large eddies being shed from the s-duct wall, which might be cut multiple times by successive blades (a similar phenomenon has been already experimentally observed by Murray et al. [20] and Alexan-

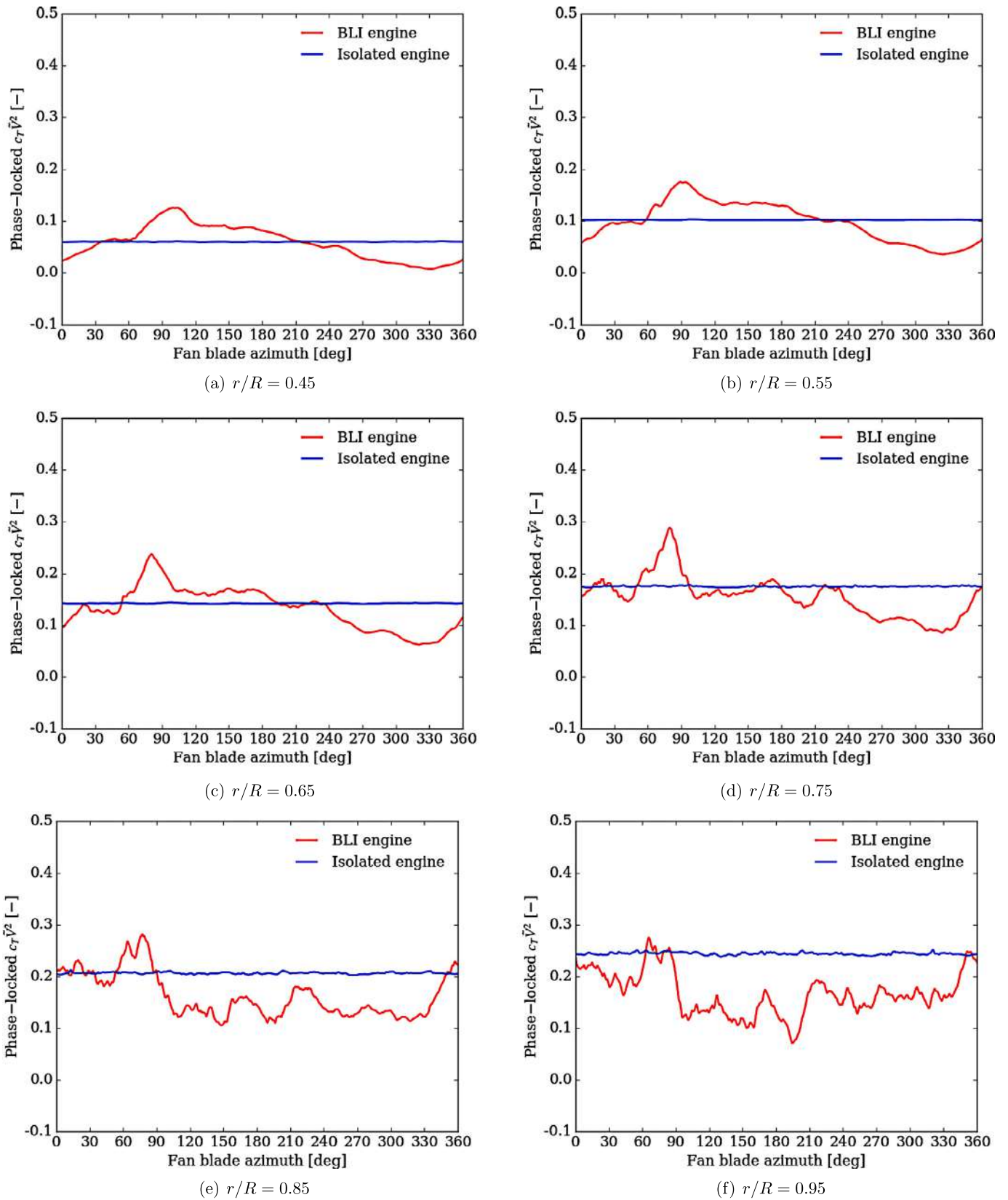


Fig. 17. Phase-locked fan blade sectional thrust coefficient time-histories at different span-wise locations.

der et al. [54] for a rotor case ingesting a planar boundary-layer). For the BLI case, broadband levels turn out to be from 10 to 20 dB overall higher than those related to the isolated configuration, for most of the frequencies and directivity angles considered. More-

over, the BLI layout appears to be as noisy as the isolated one on the sideline arc for directivity angles around 90° and frequencies higher than BPF-2 (Fig. 21(b)), or quieter by 5-10 dB on the ground arc (Fig. 21(a)). This last point might be related to some

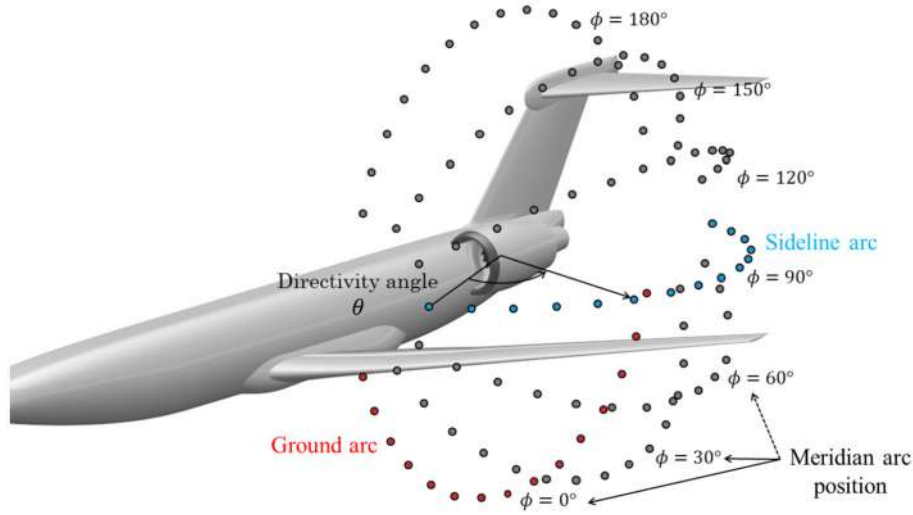


Fig. 18. Sketch of the microphone array used for far-field noise computations. The angle ϕ denotes the position of each meridian arc.

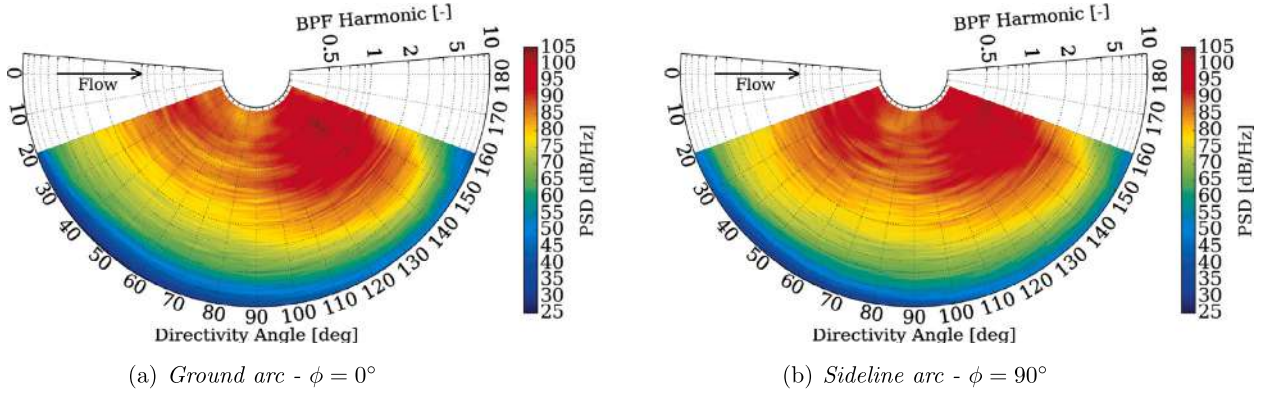


Fig. 19. Far-field noise directivity on ground (a) and sideline (b) arcs of 10 m radius and centered around the fan, BLI engine.

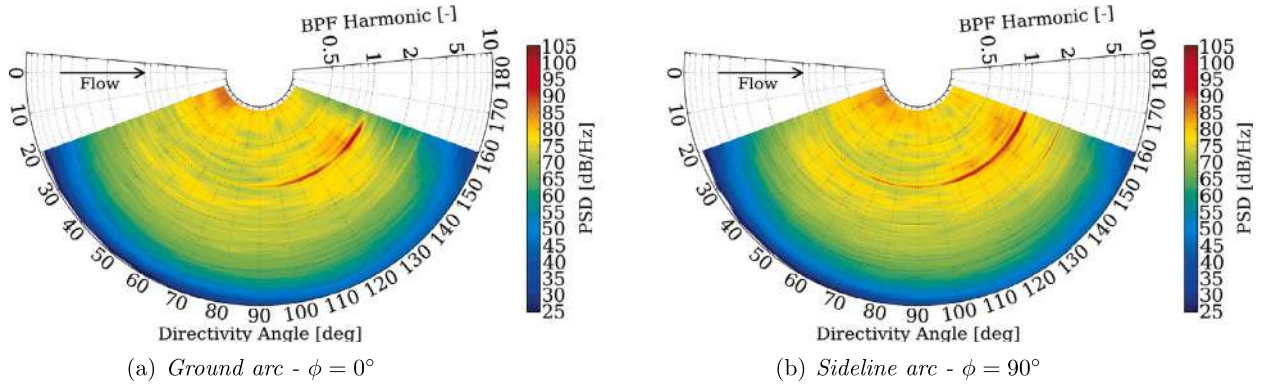


Fig. 20. Far-field noise directivity on ground (a) and sideline (b) arcs of 10 m radius and centered around the fan, isolated engine.

noise shielding effects introduced by the partial placement of the engine into the fuselage.

4.6. Noise power level

In Fig. 23 one-side narrow-band source Power Level (PWL) is presented for both BLI and isolated configuration (Fig. 23(a)). For convenience, the difference between the power levels of the two cases is also shown in Fig. 23(b). In this study, the PWL is computed by integration of the PSDs over the semi-spherical surface portion corresponding to the aforementioned microphone array,

using the following formula:

$$PWL(f) = \int_{\theta_{min}}^{\theta_{max}} \int_{\phi_{min}}^{\phi_{max}} R_s^2 \sin(\theta) \frac{[1 + M_\infty \cos(\theta)]^2 PSD(f, \theta)}{2\rho_\infty a_\infty} d\phi d\theta \quad (4)$$

where f is the frequency, R_s is the hemisphere radius, ϕ is the meridian arc angular position (defined as in Fig. 18) and varying from $\phi_{min} = 0^\circ$ to $\phi_{max} = 180^\circ$, whereas θ is the directivity angle varying from $\theta_{min} = 20^\circ$ to $\theta_{max} = 160^\circ$. Moreover, M_∞ is the free-

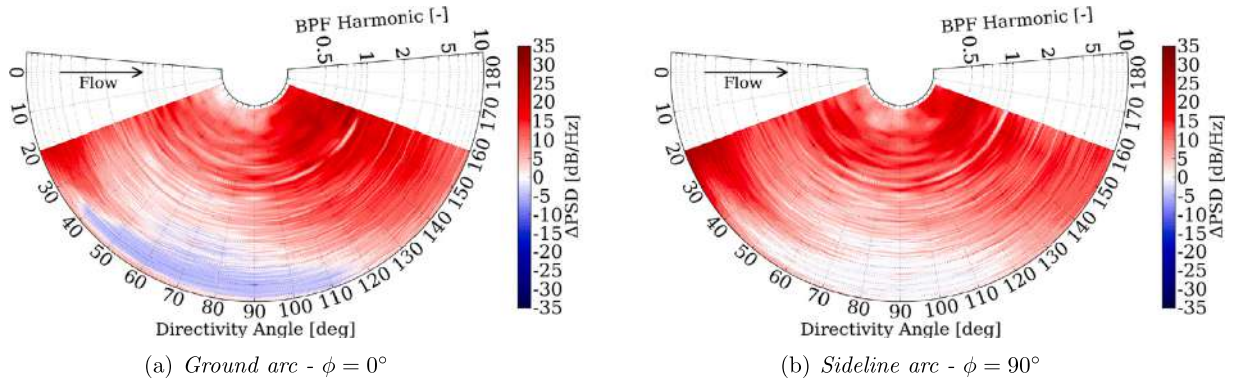


Fig. 21. Far-field noise directivity on ground (a) and sideline (b) arcs of 10 m radius and centered around the fan, difference between BLI and isolated engines.

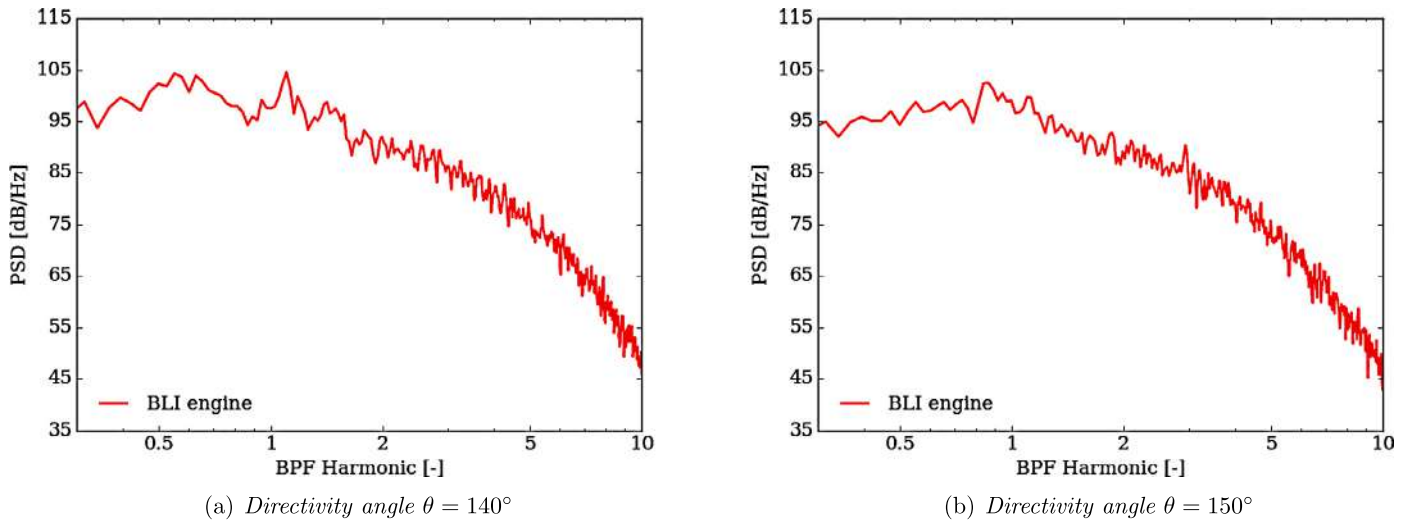


Fig. 22. Far-field noise spectra on ground arc at downstream directivity angles: 140° (a) and 150° (b), BLI engine.

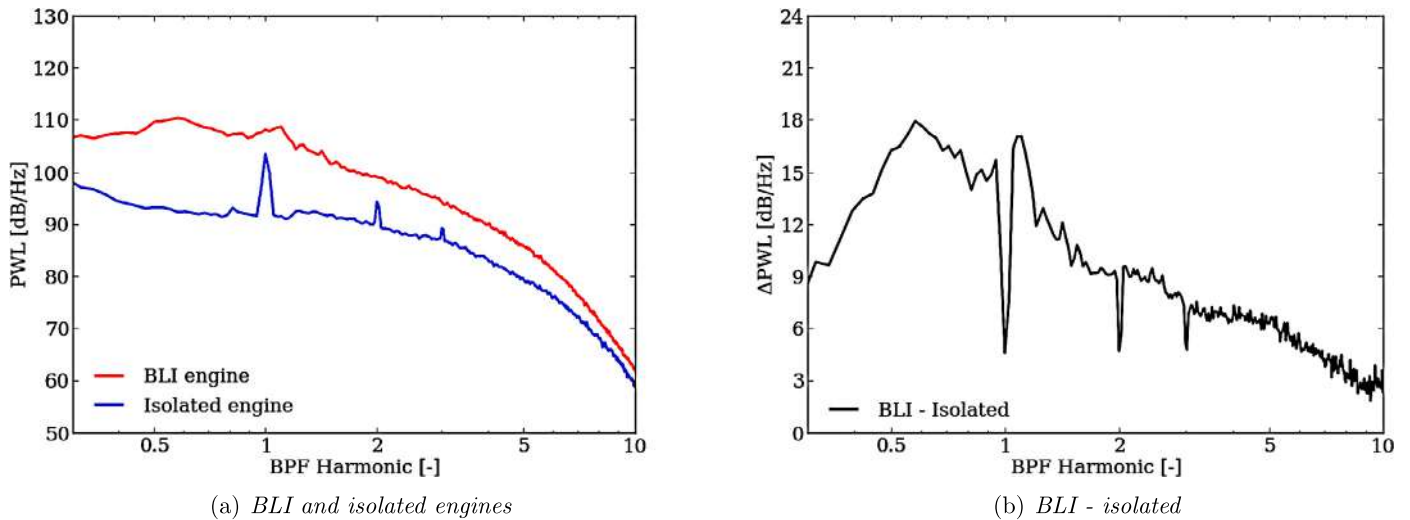


Fig. 23. Source Power Level: BLI and isolated engines (a) and their difference (b).

stream Mach number, and ρ_∞ and a_∞ are the ambient density and speed of sound, respectively.

As already observed, broadband component dominates the power level spectrum for the BLI configuration, as a consequence of the less axisymmetric rotor wakes and higher levels of turbulence impinging on the stator vanes. No tones at harmonics of

the BPF are observed, and only weak haystacked peaks around BPF-1 are found. As mentioned before, such broadened peaks might be connected to blade-to-blade unsteady airloads correlation associated to the simultaneous impingement of large vortical structures with multiple neighboring fan blades. Finally, regarding the isolated engine, the PWL presents distinct tones at the first 3

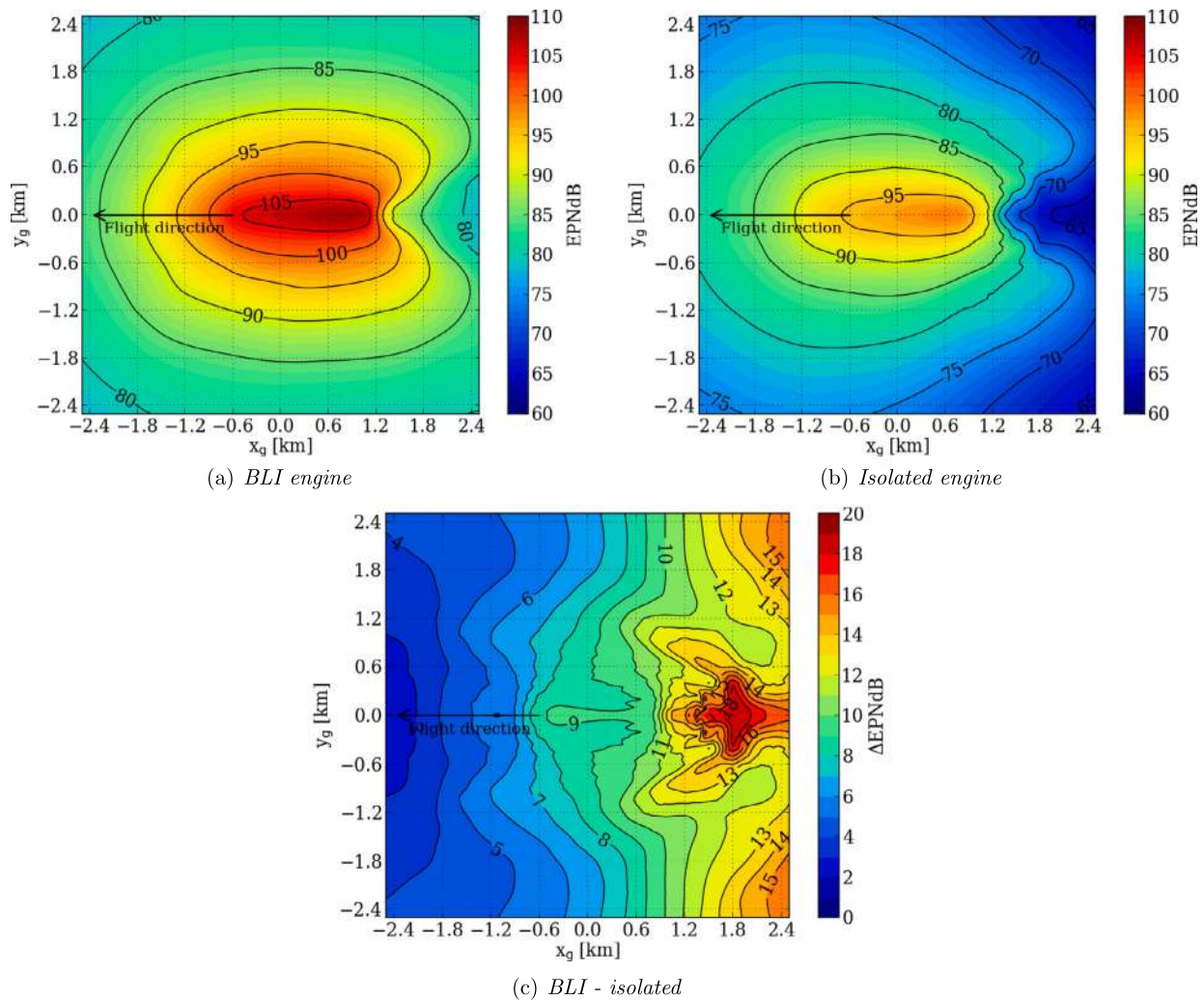


Fig. 24. EPNL on a plane 1.2 m above the ground during a take-off flight path with power cut-back: BLI engine (a), isolated engine (b) and their difference (c).

blade-passing frequencies, and lower broadband source power levels, from 4-5 dB at high frequencies up to 15-18 dB at low ones, with respect to the BLI configuration.

4.7. Effective perceived noise level

The analysis of BLI installation effects on fan noise is concluded by investigating the Effective Perceived Noise Level (EPNL) footprint during a take-off flight path with power cut-back. In the present study, the EPNL is computed (as briefly described in 2.3) according to the FAR procedure [21] by considering a rectilinear flight path of 2 km length (from $x_g = -1000$ m to $x_g = 1000$ m), 210 m altitude difference (from $z_g = 200$ m to $z_g = 410$ m) and 23.7 sec duration. The free-stream conditions applied are those presented in Sec. 3.1 and an atmospheric relative humidity of 70% is considered. Figs. 24(a) and 24(b) show the EPNL on a plane 1.2 m above the ground over an area of 2.5×2.5 km² for the BLI and isolated cases, respectively, whereas the EPNL difference between the two configurations is shown in Fig. 24(c). Since in this study simulations are performed by employing a symmetry plane located at the centerline of the aircraft, the EPNL footprint is computed by mirroring the source of noise (i.e. the noise hemisphere) with respect to the same plane (located at $y_g = 0$ m) prior to the projection of the NBN spectra on the ground microphone carpet. The two contributions of the mirrored hemispheres are added incoherently.

As expected, due to the take-off flight path considered, both the EPNL contours show that the highest noise levels take place at the beginning of the flight trajectory, i.e. when the distance between the source of noise and the ground is the minimum. Then, for both cases, the on-the-ground noise levels gradually decreases along the flight direction as the noise source altitude increases. Nevertheless, the two configurations show quite different EPNL levels and directivity patterns. First, the EPNL map is characterized by a peak value of 108 EPNdB for the BLI case, which is roughly 10 EPNdB larger than that of the isolated one (98 EPNdB). Secondly, the BLI configuration shows that the noise on the ground, during the take-off maneuver, is mainly radiated along the sideline and downstream directions, contrarily to the isolated case whose take-off noise radiation is predominantly directed upstream. Overall, the BLI case turns out to be from 4 EPNdB (front side) to 18 EPNdB (aft side) noisier than the isolated one for the operating condition hereof considered.

5. Conclusions and future outlook

For the first time, a high-fidelity CFD/CAA simulation of a full-scale aircraft geometry comprehensive of a BLI fan/OGV stage was performed. A modified version of the Low-Noise configuration of the NASA SDT fan-stage was embedded into the ONERA NOVA fuselage in order to reproduce the NOVA BLI aircraft configuration. The numerical flow solution was obtained by solving

the explicit, transient and compressible lattice-Boltzmann equation implemented in the high-fidelity CFD/CAA solver Simulia PowerFLOW®. The acoustic far-field was computed by using the Ffowcs-Williams & Hawkings integral solution applied to a permeable surface encompassing the fan-stage. Installation effects of the BLI configuration, which is not optimal, were investigated by comparison with an isolated setup of the modified Low-Noise SDT fan-stage geometry in terms of fan-stage velocity field, fan performances, fan blade unsteady airload, far-field noise and on-the-ground noise footprint. All simulations were performed for an operating condition representative of a take-off with power cut-back.

The analysis of the fan-stage velocity field showed that, for the considered operating condition and geometry, the embedded BLI fan-stage causes high levels of mean flow distortion and flow separation at approximately 60% of the s-duct length and in proximity of the fan plane on the nacelle side. The mean flow distortion was found to be responsible of a low-frequency periodic variation of the fan blade sectional thrust for inboard blade sections. The ingestion of turbulence, associated to the flow separation on the s-duct and inlet walls, led to high levels of unsteadiness, as well as to a deficit in thrust generation in outboard blade regions. A reduction of the FPR by 2.5% and of the fan isentropic efficiency by 9.2% was observed for the BLI configuration compared to the isolated one. In addition, the BLI engine interstage flow field was characterized by less axisymmetric and coherent tangential velocity variations associated to the rotor wake, and higher levels of in-plane velocity fluctuations, compared to the isolated one. Finally, the BLI configuration showed a non-uniform and lower swirl recovery downstream the stator compared to the isolated engine, as well as higher level of turbulent fluctuations.

Far-field noise directivity predictions revealed that the noise is radiated most efficiently downstream the engine for the BLI layout, as also observed for the isolated engine. However, while the latter manifested both broadband and tonal noise contributions, no tones clearly emerged with respect to broadband levels for the BLI case. Weak haystacked peaks were found around BPF-1 for downstream observer angles. Such peaks might be connected to blade-to-blade unsteady airloads correlation associated to the simultaneous impingement of large vortical structures separating from the s-duct wall and fuselage turbulent boundary-layer with multiple neighboring fan blades. Overall, the BLI configuration showed from 10 to 20 dB higher broadband levels in the far-field compared those related to the isolated configuration, for most of the frequencies and directivity angles considered. The BLI layout resulted to be by 5–10 dB quieter than the isolated one on the ground arc, for directions nearly perpendicular to the engine axis and for frequencies higher than BPF-2, as a result of some airframe shielding related to the partial placement of the engine inside the fuselage. Finally, the BLI configuration is found to have a detrimental impact on cumulative noise levels during a take-off flight with power cut-back up to 18 EPNdB.

It should be recalled that the fan stage considered in this study is designed for isolated engines, thus it is not suitable for a operate in highly distorted flows such as in BLI configurations. Moreover, the current NOVA BLI configuration represents a rather idealized BLI-layout, due to the relative short s-duct length and the large portion of intake area embedded into the fuselage. A more conservative sizing, e.g. based on a longer s-duct length and a lower percentage of buried intake, would reduce the amount of flow separation and distortion at the fan section, with expected benefits on fan-stage operability and noise emissions, however at the additional cost of higher nacelle mass, drag and inlet friction losses.

As future outlook, simulations by employing flow-control techniques will be performed for the BLI configuration in order to mitigate the flow separation over the s-duct wall and the related benefits in terms of noise emission will be assessed.

Declaration of competing interest

The authors declare no conflict of interest regarding this article.

Acknowledgements

This project is supported by the project ARTEM (Aircraft noise Reduction Technologies and related Environmental iMPact) which has received funding from the European Union's Horizon 2020 research and innovation programme under grant No. 769 350. The authors would further like to thank the Department of Aerodynamics, Aeroelasticity and Aeroacoustics of ONERA for the provision of the NOVA fuselage geometry, with wing and empennage, that was used in this study.

References

- [1] S. Kallas, M. Geoghegan-Quinn, M. Darecki, C. Edelstenne, T. Enders, E. Fernandez, P. Hartman, Flightpath 2050 Europe's Vision for Aviation, Report of the High Level Group on Aviation Research, Report No. EUR 98, European Commission, Brussels, Belgium, 2011.
- [2] C.E. Hughes, NASA Collaborative Research on the Ultra High Bypass Engine Cycle and Potential Benefits for Noise, Performance, and Emissions, Technical Memorandum TM-2013-216345, NASA, 2013.
- [3] E.M. Greitzer, P. Bonnefoy, E. De la Rosa Blanco, C. Dorbian, M. Drela, D. Hall, R. Hansman, J. Hileman, R. Liebeck, J. Levegren, et al., N+3 Aircraft Concept Designs and Trade Studies. Volume 1, Nasa CR-2010-216794/vol2, NASA Glenn Research Center, Cleveland, Ohio, 2010.
- [4] C. Heykena, L. Savoni, J. Friedrichs, R. Rudnik, Engine airframe integration sensitivities for a STOL commercial aircraft concept with over-the-wing mounted UHBR-turbofans, in: Proceedings of Montreal 2018 Global Power and Propulsion Forum, 2018.
- [5] L. Wiart, O. Atinault, R. Grenon, B. Paluch, D. Hue, Development of NOVA aircraft configurations for large engine integration studies, in: 33rd AIAA Applied Aerodynamics Conference, 2015, p. 2254.
- [6] L. Wiart, O. Atinault, J.-C. Boniface, R. Barrier, Aeropropulsive performance analysis of the NOVA configurations, in: 30th Congress of the International Council of the Aerodynamical Sciences, 2016.
- [7] A. Plas, D. Crichton, M. Sargeant, T. Hynes, E. Greitzer, C. Hall, V. Madani, Performance of a boundary layer ingesting (BLI) propulsion system, in: 45th AIAA Aerospace Sciences Meeting and Exhibit, 2007, p. 450.
- [8] M. Drela, Power balance in aerodynamic flows, *AIAA J.* 47 (7) (2009) 1761–1771.
- [9] L. Hardin, G. Tillman, O. Sharma, J. Berton, D. Arend, Aircraft system study of boundary layer ingesting propulsion, in: 48th AIAA/ASME/SAE/ASEE Joint Propulsion Conference & Exhibit, 2012, p. 3993.
- [10] G. Carrier, O. Atinault, R. Grenon, C. Verbecke, Numerical and experimental aerodynamic investigations of boundary layer ingestion for improving propulsion efficiency of future air transport, in: 31st AIAA Applied Aerodynamics Conference, 2013, p. 2406.
- [11] K.M. Sabo, M. Drela, Benefits of boundary layer ingestion propulsion, in: 53rd AIAA Aerospace Sciences Meeting, 2015, p. 1667.
- [12] P. Lv, D. Ragni, T. Hartuc, L. Veldhuis, A. Rao, Experimental investigation of the flow mechanisms associated with a wake-ingesting propulsor, *AIAA J.* (2016) 1332–1342.
- [13] P. Lv, A.G. Rao, D. Ragni, L. Veldhuis, Performance analysis of wake and boundary-layer ingestion for aircraft design, *J. Aircr.* 53 (5) (2016) 1517–1526.
- [14] A. Uranga, M. Drela, E.M. Greitzer, D.K. Hall, N.A. Titchener, M.K. Lieu, N.M. Siu, C. Casses, A.C. Huang, G.M. Gatlin, et al., Boundary layer ingestion benefit of the D8 transport aircraft, *AIAA J.* (2017) 3693–3708.
- [15] A. Anabaw, R. Blackwelder, P. Lissaman, R. Liebeck, An experimental investigation of boundary layer ingestion in a diffusing S-duct with and without passive flow control, in: 37th Aerospace Sciences Meeting and Exhibit, 1999, p. 739.
- [16] S. Gorton, L. Owens, L. Jenkins, B. Allan, E. Schuster, Active flow control on a boundary-layer-ingesting inlet, in: 42nd AIAA Aerospace Sciences Meeting and Exhibit, 2004, p. 1203.
- [17] L.R. Owens, B.G. Allan, S.A. Gorton, Boundary-layer-ingesting inlet flow control, *J. Aircr.* 45 (4) (2008) 1431–1440.
- [18] J.J. Defoe, Z.S. Spakovszky, Effects of boundary-layer ingestion on the aeroacoustics of transonic fan rotors, *J. Turbomach.* 135 (5) (2013) 051013.
- [19] I. Clark, R.H. Thomas, Y. Guo, Aircraft system noise assessment of the NASA D8 subsonic transport concept, in: 2018 AIAA/CEAS Aeroacoustics Conference, 2018, p. 3124.
- [20] H.H. Murray, W.J. Devenport, W.N. Alexander, S.A. Glegg, D. Wisda, Aeroacoustics of a rotor ingesting a planar boundary layer at high thrust, *J. Fluid Mech.* 850 (2018) 212–245.

- [21] U.S. Department of Transportation (DOT), Federal Aviation Administration (FAA), Code of Federal Regulation (CFR) - Title 14: Aeronautics and Space - Part 36. Noise Standards: Aircraft Type and Airworthiness Certification - Subpart B: Noise Levels for Transport Category and Jet Airplanes (1969 onwards).
- [22] F. Avallone, W. Van der Velden, D. Ragni, D. Casalino, Noise reduction mechanisms of sawtooth and combed-sawtooth trailing-edge serrations, *J. Fluid Mech.* 848 (2018) 560–591.
- [23] W.C.P. van der Velden, D. Casalino, P. Gopalakrishnan, A. Jammalamadaka, Y. Li, R. Zhang, H. Chen, Validation of jet noise simulations and resulting insights of acoustic near field, *AIAA J.* (2019) 1–12, <https://doi.org/10.2514/1.j057970>.
- [24] G. Romani, D. Casalino, Rotorcraft blade-vortex interaction noise prediction using the Lattice-Boltzmann method, *Aerosp. Sci. Technol.* 88 (2019) 147–157.
- [25] F. Avallone, D. Casalino, D. Ragni, Impingement of a propeller slipstream on a leading edge with a flow-permeable insert: a computational aeroacoustic study, *Int. J. Aeroacoust.* 17 (6–8) (2018) 687–711.
- [26] D. Casalino, A.F.P. Ribeiro, E. Fares, S. Nölting, Lattice-Boltzmann aeroacoustic analysis of the lagoon landing gear configuration, *AIAA J.* 52 (6) (2014) 1232–1248.
- [27] D. Casalino, A.F.P. Ribeiro, E. Fares, Facing rim cavities fluctuation modes, *J. Sound Vib.* 333 (13) (2014) 2812–2830.
- [28] M.R. Khorrami, E. Fares, D. Casalino, Towards Full Aircraft Airframe Noise Prediction: Lattice Boltzmann Simulations, *AIAA Paper 2014-2481*, 2014.
- [29] E. Fares, D. Casalino, M. Khorrami, Evaluation of Airframe Noise Reduction Concepts Via Simulations Using a Lattice Boltzmann Approach, *AIAA Paper 2015-2988*, 2015.
- [30] D. Casalino, A. Hazir, A. Mann, Turbofan broadband noise prediction using the lattice Boltzmann method, *AIAA J.* 56 (2) (2017) 609–628.
- [31] I. Gonzalez-Martino, D. Casalino, Fan tonal and broadband noise simulations at transonic operating conditions using lattice-Boltzmann methods, in: 2018 AIAA/CEAS Aeroacoustics Conference, 2018, p. 3919.
- [32] E. Envia, Fan Noise Source Diagnostic Test-Vane Unsteady Pressure Results, *AIAA Paper 2002-2430*, 2002.
- [33] H. Chen, S. Kandasamy, S.A. Orszag, S. Succi, V. Yakhot, Extended Boltzmann kinetic equation for turbulent flows, *Science* 301 (5633) (2003) 633–636.
- [34] H. Chen, S. Orszag, I. Staroselsky, S. Succi, Expanded analogy between Boltzmann kinetic theory of fluid and turbulence, *J. Fluid Mech.* 519 (2004) 301–314.
- [35] V. Yakhot, S.A. Orszag, Renormalization group analysis of turbulence. I. Basic theory, *J. Sci. Comput.* 1 (1) (1986) 3–51.
- [36] V. Yakhot, S.A. Orszag, S. Thangam, T.B. Gatski, C.G. Speziale, Development of turbulence models for shear flows by a double expansion technique, *Phys. Fluids A* 4 (7) (1992) 1510–1520.
- [37] X. Nie, X. Shan, H. Chen, A Lattice-Boltzmann/Finite-Difference Hybrid Simulation of Transonic Flow, *AIAA Paper 2009-0139*, 2009.
- [38] H. Chen, S. Chen, W. Matthaeus, Recovery of the Navier-Stokes equations using a lattice-gas Boltzmann method, *Phys. Rev. A* 45 (8) (1992) 5339–5342.
- [39] P.L. Bhatnagar, E.P. Gross, M. Krook, A model for collision processes in gases. I. Small amplitude processes in charged and neutral one-component systems, *Phys. Rev.* 94 (3) (1954) 511–525.
- [40] R. Zhang, C. Sun, Y. Li, R. Satti, R. Shock, J. Hoch, H. Chen, Lattice Boltzmann approach for local reference frames, *Commun. Comput. Phys.* 9 (5) (2011) 1193–1205.
- [41] G. Tabor, A. Gosman, R. Issa, Numerical Simulation of the Flow in a Mixing Vessel Stirred by a Rushton Turbine, Institution of Chemical Engineers Symposium Series, vol. 140, Citeseer, 1996, pp. 25–34.
- [42] H. Chen, C. Teixeira, K. Molvig, Realization of fluid boundary conditions via discrete Boltzmann dynamics, *Int. J. Mod. Phys. C* 9 (8) (1998) 1281–1292.
- [43] G.A. Brès, F. Pérot, D.M. Freed, Properties of the Lattice-Boltzmann Method for Acoustics, *AIAA Paper 2009-3395*, 2009.
- [44] G.A. Brès, F. Pérot, D.M. Freed, A Ffowcs Williams-Hawkings Solver for Lattice-Boltzmann Based Computational Aeroacoustics, *AIAA Paper 2010-3711*, 2010.
- [45] D. Casalino, An advanced time approach for acoustic analogy predictions, *J. Sound Vib.* 261 (4) (2003) 583–612.
- [46] F. Farassat, G.P. Succi, The prediction of helicopter discrete frequency noise, *Vertica* 7 (4) (1983) 309–320.
- [47] D. Casalino, S. Noelting, E. Fares, T. Van de Ven, F. Pérot, G.A. Brès, Towards Numerical Aircraft Noise Certification: Analysis of a Full-Scale Landing Gear in Fly-Over Configuration, *AIAA Paper 2012-2235*, 2012.
- [48] W. van der Velden, A. van Zuijlen, A. de Jong, D. Ragni, Flow and self-noise around bypass transition strips, *Noise Control Eng. J.* 65 (5) (2017) 434–445.
- [49] J. Jeong, F. Hussain, On the identification of a vortex, *J. Fluid Mech.* 285 (1995) 69–94.
- [50] H. Schlichting, K. Gersten, *Boundary-Layer Theory*, Springer, 2016.
- [51] P. Klebanoff, Characteristics of Turbulence in a Boundary Layer With Zero Pressure Gradient, Tech. rep., National Bureau of Standards, Gaithersburg, MD, 1955.
- [52] G. Podboy, M. Krupar, S. Helland, C. Hughes, Steady and unsteady flow field measurements within a NASA 22 inch fan model, in: 40th AIAA Aerospace Sciences Meeting & Exhibit, 2002, p. 1033.
- [53] L.V. Lopes, D.D. Boyd Jr, D.M. Nark, K.E. Wiedemann, Identification of spurious signals from permeable Ffowcs Williams and Hawkings surfaces, in: 73rd American Helicopter Society Annual Forum, Fort Worth, Texas, USA, 2017.
- [54] W.N. Alexander, W.J. Devenport, S.A. Glegg, Noise from a rotor ingesting a thick boundary layer and relation to measurements of ingested turbulence, *J. Sound Vib.* 409 (2017) 227–240.